

MambaEviScrib: Mamba and Evidence-Guided Consistency Enhance CNN Robustness for Scribble-Based Weakly Supervised Ultrasound Image Segmentation

Xiaoxiang Han^{a,b,1}, Xinyu Li^{c,1}, Jiang Shang^{a,b}, Yiman Liu^{d,e}, Keyan Chen^c, Shugong Xu^a, Qiaohong Liu^{f,*}, Qi Zhang^{a,b,*}

^a*School of Communication and Information Engineering, Shanghai University, Shanghai, 200444, P.R.China*

^b*The SMART (Smart Medicine and AI-based Radiology Technology) Lab, Shanghai Institute for Advanced Communication and Data Science, Shanghai University, Shanghai, 200444, P.R.China*

^c*School of Health Science and Engineering, University of Shanghai for Science and Technology, Shanghai, 200093, P.R.China*

^d*Department of Pediatric Cardiology, Shanghai Children's Medical Center, School of Medicine, Shanghai Jiao Tong University, Shanghai, 200127, P.R.China*

^e*Shanghai Engineering Research Center of Intelligence Pediatrics (SERCIP), Shanghai, 200127, P.R.China*

^f*School of Medical Instruments, Shanghai University of Medicine and Health Sciences, Shanghai, 201318, P.R.China*

Abstract

Segmenting anatomical structures and lesions from ultrasound images contributes to disease assessment, diagnosis, and treatment. Weakly supervised learning (WSL) based on sparse annotation has achieved encouraging performance and demonstrated the potential to reduce annotation costs. This study attempts to introduce scribble-based WSL into ultrasound image segmentation tasks. However, ultrasound images often suffer from poor contrast and unclear edges, coupled with insufficient supervision signals for edges, posing challenges to edge prediction. Uncertainty modeling has been proven to facilitate models in dealing with these issues. Nevertheless, existing uncertainty estimation paradigms are not robust enough and often filter out predictions near decision boundaries, resulting in unstable edge predictions. Therefore, we propose leveraging predictions near decision boundaries effectively. Specifically, we introduce Dempster-Shafer Theory (DST) of evidence to design an Evidence-Guided Consistency (EGC) strategy. This strategy utilizes high-evidence predictions, which are more likely to occur near high-density regions, to guide the optimization of low-evidence predictions that may appear near decision boundaries. Furthermore, the diverse sizes and locations of lesions in ultrasound images pose a challenge for convolutional neural networks (CNNs) with local receptive fields, as they struggle to model global information. Therefore, we introduce Visual Mamba based on structured state space sequence models, which achieves long-range dependency with linear computational complexity, and we construct a novel hybrid CNN-Mamba framework. During training, the collaboration between the CNN branch and the Mamba branch in the proposed framework draws inspiration from each other based on the EGC strategy. Extensive experiments on four ultrasound public datasets for binary-class and multi-class segmentation demonstrate the competitiveness of the proposed method. The scribble-annotated dataset and code will be made available on <https://github.com/GtLinyer/MambaEviScrib>.

Keywords: Weakly supervised learning, Mamba, Evidential Deep Learning, Image Segmentation, Ultrasound

*Corresponding Authors.

Email addresses: hanxx@shu.edu.cn (Xiaoxiang Han),

1. Introduction

Medical ultrasound imaging holds a pivotal position in the field of medical diagnosis. Segmenting anatomical structures and lesions from ultrasound images plays an essential role in computer-aided diagnosis (CAD) system. It can provide valuable reference information for clinicians, such as the morphology, size, location, and relationship with surrounding tissues of organs or lesions [1]. With the advancement of deep learning (DL) [2, 3, 4], significant progress has been made in medical image segmentation [5, 6]. Generally, supervised learning methods for segmentation require large-scale pixel-wise annotated data to effectively train accurate models. However, the annotation of medical ultrasound images differs from that of natural images, requiring specialized medical expertise. Consequently, pixel-level annotation of large-scale ultrasound images is both costly and time-consuming.

To address this challenge, researchers have devoted themselves to developing DL technologies that do not rely on precise dense annotations, such as weakly supervised learning (WSL) [7, 8, 9], semi-supervised learning [10], and self-supervised learning [11, 4]. This study focuses on exploring WSL method based on scribble annotations. The sparse annotation adopted by this method is easier to obtain compared to dense annotation, and offers greater convenience, versatility, and adaptability than other sparse annotation methods [12]. As depicted in Fig. 1 (a), by providing masks in the form of scribbles, which annotate only a small portion of pixels, this method can effectively reduce annotation costs and improve annotation efficiency. Given that a scribble represents a minute subset of the region of interest, the primary challenge in weakly supervised segmentation relying on scribble annotations stems from the inadequacy of training supervision information. To effectively leverage the information from unlabeled pixels, consistency regularization [13, 14] has emerged as the most prevalent strategy. This regularization is grounded in the smoothness assumption, which posits that if two points, x_1 and x_2 , are close in a high-density region, their corresponding outputs, y_1 and y_2 ,

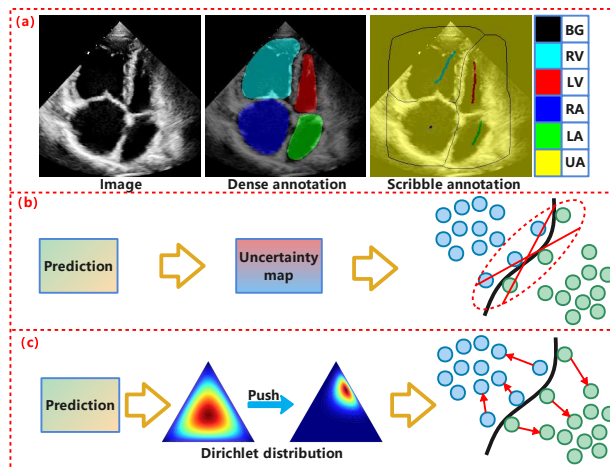


Figure 1: (a) Examples of the dense annotation and the scribble annotation. BG, RV, LV, RA, LA, and UA represent the background, right ventricle, left ventricle, right atrium, left atrium, and unannotated pixels respectively. (b) Existing uncertainty estimation methods typically discard predictions located near the decision boundary. (c) The evidence-guided consistency strategy leverages the robust evidential deep learning to guide predictions near the decision boundary towards high confidence based on evidence.

should also be close. Rather than directly computing distances between different input samples (which is challenging), consistency regularization synthesizes new input samples, x' , from the original input samples, x , where the proximity of x and x' in a semantically meaningful space is known. This approach allows the model to understand which unlabeled pixels are semantically close to labeled pixels. However, enforcing consistency in predictions across all pixels is unreasonable, as high-confidence predictions may be biased by low-confidence ones.

This prompts us to rethink the paradigm of consistency regularization. Existing methods [15] propose uncertainty estimation, then discard unreliable predictions near the decision boundary. However, considering the issues of poor contrast and unclear edges in ultrasound images, this may compromise the stability of segmentation edge predictions. Therefore, we explore how to leverage uncertainty effectively, neither enforcing uniformity in all pixel predictions nor discarding marginal decisions. Inspired by clinical consultations, clinicians with diverse backgrounds may have varying levels of confidence in their judgments based on past experience. When disagree-

xinyuli_01@163.com (Xinyu Li), liuqh@sumhs.edu.cn (Qiaohong Liu), zhangq@t.shu.edu.cn (Qi Zhang)

¹These authors contributed equally to the work, and are co-first authors.

ments arise, clinicians with high confidence can guide and enhance the confidence of those with lower confidence. Therefore, let us regard disagreements as a treasure to address the aforementioned issues. Moreover, there are two key issues to address: Firstly, how can we estimate uncertainty elegantly and robustly? Secondly, how can we construct two experts with different strengths? This is because uncertainty estimation requires evidence to support whether it stems from the model’s inherent knowledge limitations. Additionally, constructing experts with different strengths depends on the varying sizes and locations of lesions in ultrasound images, necessitating both local and global receptive fields.

To this end, we propose a novel scribble-based weakly supervised approach for ultrasound image segmentation, called **MambaEviScrib**, which comprises dual branch networks, i.e., the **CNN and Mamba** branches. CNN and Mamba serve as two experts with distinct advantages, where the CNN branch captures local information while the Mamba branch is responsible for capturing global features and maintaining linear computational complexity. We then introduce Dempster-Shafer Theory (DST) of evidence, utilizing the Dirichlet distribution to parameterize the probability distribution of segmentation probabilities, i.e., second-order probabilities, and estimate uncertainty. An **Evidence-Guided Consistency (EGC) strategy** is proposed, leveraging high-evidence predictions more likely to occur near high-density regions to guide the optimization of confidence in low-evidence predictions that may appear near decision boundaries. This strategy focuses on guiding low-confidence predictions towards high confidence rather than directly enforcing consistency among divergent predictions, which contributes to the robustness and credibility of the model and enhances the stability of edge predictions. Furthermore, we design a partial evidential deep learning (pEDL) loss function for the optimization of second-order probabilities. We optimize the weakly supervised loss function, to leverage both the supervision information and the structural information to better handle edges.

Extensive experiments were conducted to validate MambaEviScrib on four public ultrasound datasets: CardiacUDA [16], EchoNet [17], BUSI [18] and DDTI [19]. **Note** that our approach employs only U-Net in the inference stage, and we have made no modifications to U-Net. Therefore, we enjoy a superior inference efficiency com-

pared to other complex models.

The main contributions of this paper are as follows.

1. We propose a dual-branch scribble-based weakly supervised segmentation framework comprising CNN and Mamba, which respectively extract local and global features from ultrasound images.
2. The EGC strategy is developed to fully leverage predictions near decision boundaries, enhancing the stability of edge segmentation and the robustness of the model.
3. We design a pEDL loss function, and the supervised loss functions co-optimize the generation of pseudo-labels using the features of input images and ground truth, further enhancing edge segmentation performance.
4. To our best knowledge, we are the first to apply scribble-based WSL for ultrasound image segmentation. We will publicly release four ultrasound datasets along with their scribble annotations, as well as our code.

2. Related Works

2.1. DL-based ultrasound image segmentation

With extensive research on DL in the field of medical image segmentation [5, 6], this technology has rapidly been applied to ultrasound image segmentation. However, compared with imaging techniques such as CT and MRI, ultrasound images typically have lower contrast and clarity, as well as abundant noise and artifacts, posing challenges for clinicians in analyzing and diagnosing medical conditions [20]. Accurate segmentation of anatomical structures and lesions can be of great assistance. Initially, the DL-based methods primarily relied on CNN architectures. For instance, Leclerc et al. [21] evaluated that U-Net and its variants outperformed traditional methods in multi-structure ultrasound segmentation. Furthermore, some novel CNN-based network architectures [22, 23] were proposed, demonstrating superior performance in ultrasound image segmentation. Liu et al. [24] innovatively introduced a pyramid local attention mechanism to enhance features within compact and sparse regions. The Transformer-based approach benefits from the global attention mechanism, facilitating a more comprehensive capture of contextual information within images [6]. Li

et al. [25] refined the Transformer architecture, effectively reducing model complexity while enhancing segmentation accuracy, demonstrating superior performance in the segmentation of both ultrasound and pathological images. The hybrid architecture of Transformer and CNN represents a more prevalent approach for improvement, leveraging their respective strengths to achieve success in segmenting a variety of lesions from ultrasound images [26, 27]. For instance, Yang et al. [28] devised various strategies to integrate CNN and Swin-Transformer, demonstrating a competitive performance in breast lesion segmentation on ultrasound images. The recently popular Mamba [29, 30, 31], owing to its linear complexity, is poised to replace Transformer. There have been some preliminary applications of ultrasound image segmentation [32, 33], for instance, Ye et al. [34] introduced shape perception to apply Mamba in segmenting the left ventricle from pediatric echocardiography. However, the aforementioned methods are all based on supervised learning, which requires large-scale dense annotations, leading to high time and labor costs. Therefore, this paper attempts to alleviate this issue in ultrasound image segmentation.

2.2. Weakly supervised medical image segmentation

Weakly supervised medical image segmentation utilizes weak annotations such as points [8], lines [9], and bounding boxes [35] to reduce the complexity and cost of data annotation while ensuring segmentation performance. Due to their convenience and versatility, scribble-based methods have gained popularity and achieved success in medical image segmentation [9]. Lin et al. [36] conducted an early attempt by developing a graphical model that propagates information jointly from scribbles to unlabeled pixels and learns network parameters. The gated CRF loss function proposed by Obukhov et al. [37] for training unlabeled pixels aided in precise segmentation of boundaries. Lee et al. [38] combined pseudo-labeling with label filtering to enhance the reliability of label generation. Luo et al. [9] proposed a dynamic mixed pseudo-labeling method, which has achieved advantages in MR image segmentation. Furthermore, Li et al. [39] proposed ScribbleVC, which leverages vision and class embeddings via the multimodal information enhancement mechanism, unifying CNN and Transformer features for better visual feature extraction. Subsequently, they proposed ScribbleFormer, comprising three branches: a CNN

branch, a Transformer branch, and an attention-guided class activation map (ACAM) branch, harnessing both local and global information [40]. However, most methods failed to make good use of the global information in images, and the computational cost of Transformer is relatively high. Mamba, with its distinct advantages, shows great potential.

2.3. Uncertainty estimation and evidential deep learning

Given the insufficiency of supervision information, the WSL method introduces uncertainty techniques to filter out unreliable predictions, thereby enhancing prediction reliability. For instance, Pan et al. [41] proposed holistic operations, applying multiple manipulations to neural representations to reduce uncertainties. Liu et al. [42] introduced uncertainty measurement based on Monte Carlo Dropout, enabling the calculation of consistency loss to focus solely on reliable regions. However, most methods directly discard predictions with low confidence, which may lead to inaccurate segmentation in regions such as edges. Additionally, the exclusivity of the softmax function poses difficulties in adequately describing the uncertainty within the current system.

Evidential deep learning (EDL), proposed by Sensoy et al. [43], aims to address the problem of out-of-distribution (OOD) samples by parameterizing the Dirichlet concentration distribution based on Dempster-Shafer theory of evidence (DST) and Subjective Logic (SL) theory [44]. For controversial samples, EDL tends to provide high uncertainty rather than making incorrect predictions. Chen et al. [45] proposed that EVIL enhances the credibility of semi-supervised medical image segmentation based on the aforementioned theories, yet they discarded pixels with low confidence levels.

3. Method

We define the 2D grayscale image of a B-mode ultrasound scan as $\mathbf{X} \in \mathbb{R}^{W \times H}$, where W and H represent the width and height of the image respectively. The goal of weakly supervised segmentation is to identify the class each pixel $k \in \mathbf{X}$ belongs to, thereby forming the semantic label map $\widehat{\mathbf{Y}} \in \{0, 1, \dots, K\}^{W \times H}$, where $K = 0$ represents the background class and $K > 0$ indicates the target class. We utilize a dataset $\mathcal{D} = \{(\mathbf{X}_i, \mathbf{Y}_i)\}_{i=1}^N$ containing

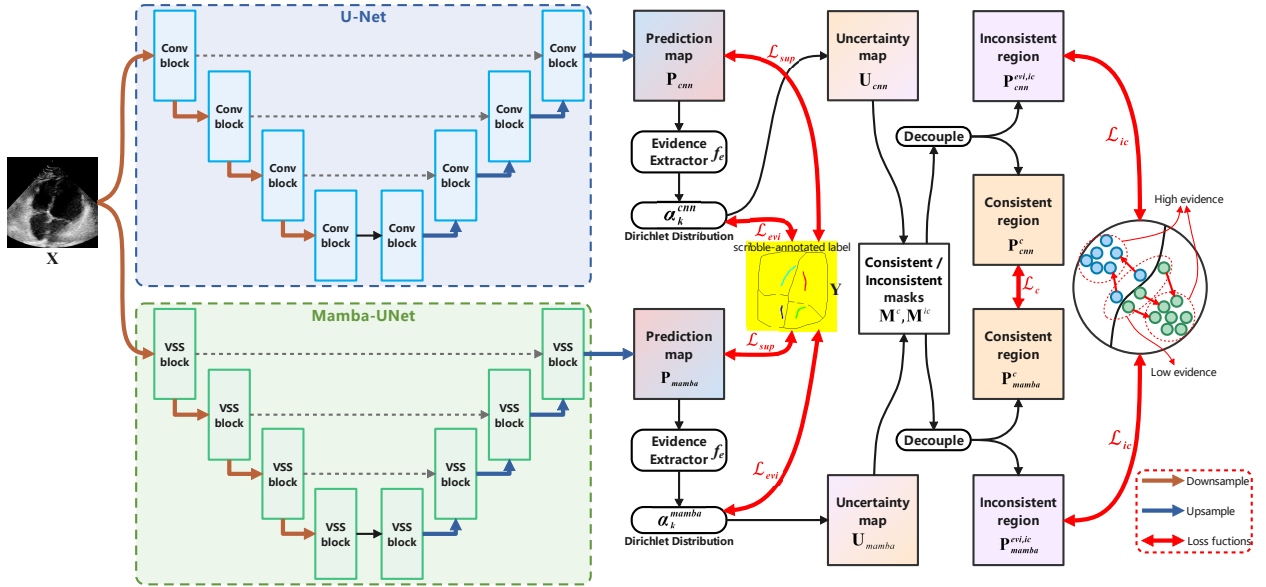


Figure 2: The pipeline of the proposed approach. The branch network in the blue box is a U-Net based on CNN architecture, and the branch network in the green box is a Mamba-UNet based on Mamba architecture. The right half presents the evidence extraction process along with the EGC strategy. The rightmost circle illustrates that samples near the decision boundary are of low evidence, whereas those in high-density regions are of high evidence.

N samples for training, where \mathbf{X}_i represents the input image and \mathbf{Y}_i denotes the scribble annotation. In the context of multi-class segmentation, \mathbf{Y}_i contains $K + 1$ categories of labels: 0 denotes unlabeled pixels, $1 \sim K - 1$ represent target pixels, and K signifies background pixels. Our framework includes a U-Net and a Mamba-UNet [46], and their parameters are randomized before training. Before feeding the images into the models, they undergo transformations including rotation, flipping, and color jittering. The outputs of the two networks are optimized with the EGC strategy. Furthermore, the evidence loss function and gated CRF loss function are employed to optimize the generation of pseudo labels. The details are elaborated subsequently. The proposed pipeline is illustrated in Fig. 2.

3.1. CNN-Mamba dual-branch network

Two network branches, U-Net and Mamba-UNet, are denoted as $\mathcal{F}_{cnn}(\cdot; \Theta_{cnn})$ and $\mathcal{F}_{mamba}(\cdot; \Theta_{mamba})$, respectively, and are highlighted in blue and green in Fig. 2. The input image \mathbf{X} is fed into two networks separately

to obtain predictions $\mathbf{P}_{cnn}, \mathbf{P}_{mamba} \in \mathbb{R}^{K \times W \times H}$. The whole process is expressed succinctly as:

$$\mathbf{P}_{cnn} = \mathcal{F}_{cnn}(\mathbf{X}; \Theta_{cnn}), \quad (1)$$

$$\mathbf{P}_{mamba} = \mathcal{F}_{mamba}(\mathbf{X}; \Theta_{mamba}), \quad (2)$$

where Θ_{cnn} and Θ_{mamba} represent the learnable parameters of the network. UNet [5], as a classic network for medical image segmentation, has been studied for a long time, offering good performance and computational efficiency. However, UNet, based on CNN, lacks the capability of capturing global information, which is enhanced under the guidance of Mamba-UNet [46]. Mamba-UNet is based on Mamba, which possesses both the ability to capture global information and linear complexity.

3.1.1. CNN branch

As U-Net is widely recognized, we just give a brief introduction. The U-Net architecture, shaped like the letter 'U', comprises an encoder and a decoder. The encoder consists of multiple convolutional blocks coupled

with pooling layers for downsampling, where each convolutional block typically incorporates 3×3 convolutions, Batch Normalization, and either ReLU or LeakyReLU activation functions. The decoder, in turn, is structured with similar convolutional blocks as well as transposed convolutional layers for upsampling. Furthermore, Each layer in the decoder is connected to its corresponding layer in the encoder through Skip Connections.

3.1.2. Mamba branch

Recently, with the introduction and advancement of State Space Models (SSM) and Structured SSM (S4) [47], their efficient performance in handling long sequences holds promise as a cost-effective alternative to the high-cost Transformers.

Traditional SSMs, as functions of linear time-invariant systems, consist of a state equation and an observation equation, which are formulated as linear ordinary differential equations (ODEs). The state equation depicts how the system’s state variables evolve over time. It typically encompasses the current state, inputs, and possibly system parameters. Mathematically, the state equation can be expressed as:

$$h'(t) = \mathbf{A}h(t) + \mathbf{B}x(t), \quad (3)$$

where $h(t) \in \mathbb{R}^N$ represents the system state at time step t , $h'(t)$ denotes the derivative of the state vector $h(t)$ with respect to step t , $x(t) \in \mathbb{R}$ is the input at time step t , $\mathbf{A} \in \mathbb{R}^{N \times N}$ is the state transition matrix, and $\mathbf{B} \in \mathbb{R}^N$ is the input control matrix. The observation equation characterizes the relationship between the system output and its state, which can be mathematically expressed as:

$$y(t) = \mathbf{C}h(t) + \mathbf{D}x(t), \quad (4)$$

where $y(t) \in \mathbb{R}$ represents the system output at time step t , $\mathbf{C} \in \mathbb{R}^N$ is the output matrix, and $\mathbf{D} \in \mathbb{R}^1$ is the direct feedthrough matrix, which characterizes how the input signal directly influences the output.

By introduced the time-scale parameter Δ , the parameters \mathbf{A} and \mathbf{B} can be discretized using the zero-order hold (ZOH) method, as defined below:

$$\bar{\mathbf{A}} = e^{\Delta\mathbf{A}}, \text{ and } \bar{\mathbf{B}} = (\Delta\mathbf{A})^{-1} (e^{\Delta\mathbf{A}} - \mathbf{I}) \cdot \Delta\mathbf{B}. \quad (5)$$

The discretized formula of the SSMs is expressed as follows:

$$h'(t) = \bar{\mathbf{A}}h(t) + \bar{\mathbf{B}}x(t), \quad (6)$$

$$y(t) = \mathbf{C}h(t) + \mathbf{D}x(t). \quad (7)$$

S4 is a discretized version of SSM that introduces the highly oscillatory partial differential equation (HIPPO) matrix to address the problem of long-range dependencies, while utilizing low-rank factorization to reduce computational complexity. It employs a convolutional architecture to represent the discretized SSM, which can be formulated as follows:

$$\bar{\mathbf{K}} = \left(\bar{\mathbf{C}}\mathbf{B}, \bar{\mathbf{C}}\mathbf{A}\mathbf{B}, \dots, \bar{\mathbf{C}}\mathbf{A}^{L-1}\mathbf{B} \right), \quad (8)$$

$$y = x * \bar{\mathbf{K}}, \quad (9)$$

where $\bar{\mathbf{K}} \in \mathbb{R}^L$ denotes the structured convolutional kernel, and L represents the length of the input sequence x . Mamba [29] inherits the strengths of S4, incorporating a selective mechanism and undergoing hardware optimization, thereby enhancing its performance in handling complex tasks.

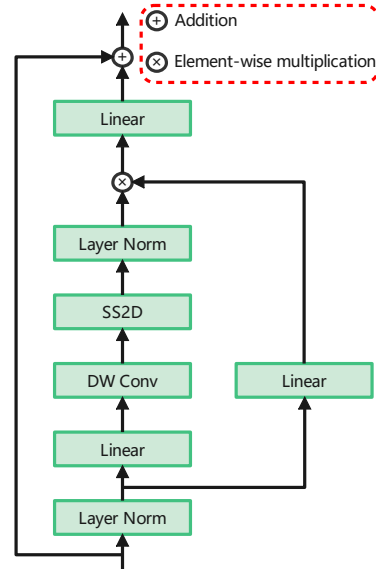


Figure 3: The concise illustration of the VSS structure. DW Conv stands for depthwise separable convolution.

VMamba [48] proposed the visual state space (VSS) block, leveraging 2D-selective-scan (SS2D) to adapt the Mamba technology into the realm of computer vision, as shown in Fig. 3. This method enables the traversal of the

spatial domain and converts non-causal visual images into ordered patch sequences, which are then processed by the SSM for each feature sequence. Subsequently, VSS has emerged as a core module for numerous visual Mambas.

In this study, we adopt Mamba-UNet [46], which resembles the U-Net architecture, as the Mamba branch network. The input 2D grayscale image of the network is first processed by a projection layer to obtain a 1-D sequence of non-overlapping patch embeddings. The input dimensions of $H \times W \times 1$ are downsampled and channel-adjusted to $\frac{H}{4} \times \frac{W}{4} \times C$. Subsequently, the patch tokens undergo feature extraction by VSS blocks, followed by downsampling and dimensionality expansion through patch merging layers. The feature maps in the encoder undergo multi-level processing, resulting in outputs with dimensions of $\frac{H}{4} \times \frac{W}{4} \times C$, $\frac{H}{8} \times \frac{W}{8} \times 2C$, $\frac{H}{16} \times \frac{W}{16} \times 4C$, and $\frac{H}{32} \times \frac{W}{32} \times 8C$, respectively. The decoder comprises VSS blocks, along with patch expanding layers designed for upsampling and dimensionality reduction. Furthermore, skip connections are employed to enhance the spatial details lost during downsampling.

3.2. Evidence-guided consistency strategy

3.2.1. Evidence and uncertainty modeling

To model evidence and uncertainty, we introduce EDL. In EDL, each pixel is assigned belief mass and uncertainty mass. We first utilize a transformation function $f_e(\cdot)$ to derive the evidence vector e_i corresponding to the i -th pixel ($i \in \{0, 1, \dots, W \times H\}$). This ensures that the evidence vector remains **non-negative**. The process is as follows:

$$e_i = f_e(\mathbf{P}_i) = e^{\tanh\left(\frac{\mathbf{P}_i}{\tau}\right)}, \quad (10)$$

where \mathbf{P}_i represents the output of the i -th pixel from the CNN or Mamba branch network, and τ denotes the scaling factor. For a segmentation task with K mutually exclusive classes (including the background class), we have $e_i = \{e_i^1, e_i^2, \dots, e_i^K\}$. The Dirichlet distribution with the parameters α_i is formulated as:

$$\alpha_i^k = e_i^k + 1, \quad (11)$$

where $k = 1, 2, \dots, K$ represents the k -th class. The Dirichlet strength S_i is defined as:

$$S_i = \sum_{k=1}^K \alpha_i^k. \quad (12)$$

The belief mass b_i^k and overall uncertainty mass u_i are formulated as:

$$b_i^k = \frac{e_i^k}{S_i}, \text{ and } u_i = \frac{K}{S_i}, \quad (13)$$

where $b_i^k \geq 0$, $u_i \geq 0$. These mass values are sum up to one, i.e.,

$$u_i + \sum_{k=1}^K b_i^k = 1. \quad (14)$$

This implies that uncertainty is inversely proportional to the total amount of evidence. When there is no evidence (i.e., $\sum e_i^k = 0$), the belief of each class is zero, and the uncertainty is one. Conversely, if the total evidence is sufficiently large, the uncertainty u_i will be small, which implies that the model has high confidence in its predictions. The prediction probability distribution for the i -th pixel is formulated by:

$$p_i^k = \frac{\alpha_i^k}{S_i}. \quad (15)$$

Thereby, the probability distributions of \mathbf{P}_{cnn} , \mathbf{P}_{mamba} are denoted as \mathbf{P}_{cnn}^{evi} , $\mathbf{P}_{mamba}^{evi} \in \mathbb{R}^{K \times W \times H}$ respectively. The Dirichlet distribution, parameterized by the evidence, represents the density of the probability distribution across the different classes predicted by the network, thereby modeling second-order probabilities and uncertainties. The Dirichlet distribution density function is formulated as:

$$D(\mathbf{p}_i | \alpha_i) = \begin{cases} \frac{1}{B(\alpha_i)} \prod_{k=1}^K (p_i^k)^{\alpha_i^k - 1} & \text{for } \mathbf{p}_i \in \mathcal{S}_K, \\ 0 & \text{otherwise,} \end{cases} \quad (16)$$

where $B(\alpha_i)$ denotes the K -dimensional multinomial beta function, and \mathcal{S}_K represents the K -dimensional unit simplex:

$$\mathcal{S}_K = \left\{ \mathbf{p} \mid \sum_{i=1}^K p_i = 1 \text{ and } 0 \leq p_1, \dots, p_K \leq 1 \right\}. \quad (17)$$

3.2.2. Evidence-guided consistency

Firstly, we need to decouple the inconsistent parts predicted by the two network branches. Given that the prediction confidence and the quality of pseudo-labels are

continually evolving during training, a dynamic threshold [49] is required to determine the regions of inconsistency. During the initial stages of training, the threshold should be kept as low as possible to facilitate the diversification of pseudo-labels. The threshold is expressed as follows:

$$\lambda_{iter} = \eta \frac{1}{B} \sum_{b=1}^B f_{max}(1 - \mathbf{U}) + (1 - \eta)\lambda_{iter-1}, \quad (18)$$

$$\eta = \frac{iter}{iter_{max}}, \quad (19)$$

where $iter$ represents the current iteration index, η is a weight that increases with the iteration of training, B denotes the batch size, $f_{max}(\cdot)$ indicates the acquisition of the maximum value, and $\mathbf{U} \in \mathbb{R}^{W \times H}$ is the normalized uncertainty map. The thresholds for \mathbf{U}_{cnn} and \mathbf{U}_{mamba} are defined as λ_{iter}^{cnn} and λ_{iter}^{mamba} respectively. To promote diversity in pseudo-labels, we select the smaller one among them as the final threshold. Furthermore, The threshold is initialized to $\frac{1}{C}$ (i.e., $\lambda_0 = \frac{1}{C}$), where C is the number of classes. Thereby, the threshold is finally adjusted as:

$$\lambda_{iter} = \begin{cases} \frac{1}{C} & iter = 0, \\ f_{min}(\lambda_{iter}^{cnn}, \lambda_{iter}^{mamba}) & \text{otherwise,} \end{cases} \quad (20)$$

where $f_{min}(\cdot)$ denotes the acquisition of the minimum value.

Next, we utilize the threshold to generate partition masks, which consist of mask $\mathcal{M}^c \in \{0, 1\}^{W \times H}$ for consistent regions and mask $\mathcal{M}^{ic} \in \{0, 1\}^{W \times H}$ for inconsistent regions:

$$\mathcal{M}^c = [(1 - \mathbf{U}) > \lambda] \wedge [(1 - \mathbf{U}) > \lambda], \quad (21)$$

$$\mathcal{M}^{ic} = \neg \mathcal{M}^c, \quad (22)$$

where \wedge denotes the logical AND operation, and \neg represents the logical NOT operation (i.e., negation). Then, the masks are employed to partition consistent regions from the predictions. The probability distribution map of the prediction probabilities for inconsistent regions is also partitioned and regarded as evidence for the subsequent EGC strategy. The processes are expressed as follow:

$$\mathbf{P}_{cnn}^c = \mathbf{P}_{cnn} \odot \mathcal{M}^c, \quad (23)$$

$$\mathbf{P}_{mamba}^c = \mathbf{P}_{mamba} \odot \mathcal{M}^c, \quad (24)$$

$$\mathbf{P}_{cnn}^{evi,ic} = \mathbf{P}_{cnn}^{evi} \odot \mathcal{M}^{ic}, \quad (25)$$

$$\mathbf{P}_{mamba}^{evi,ic} = \mathbf{P}_{mamba}^{evi} \odot \mathcal{M}^{ic}, \quad (26)$$

where \odot denotes element-wise multiplication.

Subsequently, we further decouple the inconsistent regions into predictions with low evidence that may appear near the decision boundary and predictions with high evidence that potentially occur near high-density regions. Based on the smoothness assumption, predictions from both network branches should consistently exhibit high evidence and occur near high-density regions. Consequently, we focus our efforts on optimizing probability distribution of low-evidence predictions in the vicinity of decision boundaries. The specific process is as follows: We first compare the evidence magnitudes between predictions from $\mathbf{P}_{cnn}^{evi,ic}$ and $\mathbf{P}_{mamba}^{evi,ic}$, identifying regions in $\mathbf{P}_{cnn}^{evi,ic}$ with higher evidence than those in $\mathbf{P}_{mamba}^{evi,ic}$. Subsequently, we sharpen the probability distribution of predictions in the high-evidence regions of $\mathbf{P}_{cnn}^{evi,ic}$ to bring their predictions closer to the high-density areas. Lastly, we utilize the predictions with higher evidence to guide those with lower evidence. The expression is presented as follows:

$$\mathcal{M}_{cnn}^h = \mathbf{P}_{cnn}^{evi,ic} > \mathbf{P}_{mamba}^{evi,ic}, \quad (27)$$

$$\mathbf{P}_{cnn}^{evi,ic,h} = \mathbf{P}_{cnn}^{evi,ic} \odot \mathcal{M}_{cnn}^h, \quad (28)$$

$$\mathbf{P}_{mamba}^{evi,ic,l} = \mathbf{P}_{mamba}^{evi,ic} \odot \mathcal{M}_{cnn}^h, \quad (29)$$

$$\mathbf{P}_{cnn}^{evi,ic,hh} = \left(\mathbf{P}_{cnn}^{evi,ic,h} \right)^{\frac{1}{\varepsilon}}, \quad (30)$$

where $\varepsilon \in N_{>1}$ denotes the ε -th root of $\mathbf{P}_{cnn}^{evi,ic,h}$, utilized to sharpen probability distributions with high evidence. The loss function and loss calculation for guided optimization are detailed in the next subsection.

Analogously to the aforementioned process, the regions with higher evidence in $\mathbf{P}_{mamba}^{evi,ic}$ are utilized to guide the regions with lower evidence in $\mathbf{P}_{cnn}^{evi,ic}$, which can be expressed as follows:

$$\mathcal{M}_{mamba}^h = \mathbf{P}_{mamba}^{evi,ic} > \mathbf{P}_{cnn}^{evi,ic}, \quad (31)$$

$$\mathbf{P}_{mamba}^{evi,ic,h} = \mathbf{P}_{mamba}^{evi,ic} \odot \mathcal{M}_{mamba}^h, \quad (32)$$

$$\mathbf{P}_{cnn}^{evi,ic,l} = \mathbf{P}_{cnn}^{evi,ic} \odot \mathcal{M}_{mamba}^h, \quad (33)$$

$$\mathbf{P}_{mamba}^{evi,ic,hh} = \left(\mathbf{P}_{mamba}^{evi,ic,h} \right)^{\frac{1}{\varepsilon}}. \quad (34)$$

3.3. Loss functions

The guidance optimization for EGC employs an L2 loss function, which is expressed as follows:

$$\mathcal{L}_{EGC}^a = \ell_{l2} \left[\mathbf{P}_{mamba}^{evi,ic,l}, \mathcal{O}_{detach} \left(\mathbf{P}_{cnn}^{evi,ic,hh} \right) \right], \quad (35)$$

$$\mathcal{L}_{EGC}^b = \ell_{l2} \left[\mathbf{P}_{cnn}^{evi,ic,l}, \mathcal{O}_{detach} \left(\mathbf{P}_{mamba}^{evi,ic,hh} \right) \right], \quad (36)$$

where $\mathcal{O}_{detach}(\cdot)$ denotes detachment from backpropagation, and $\ell_{l2}(\cdot, \cdot)$ represents the L2 (also known as Mean Squared Error, MSE) loss function. Thereby, the loss calculation for the inconsistent region, constrained by the EGC strategy, is as follows:

$$\mathcal{L}_{ic} = \mathcal{L}_{EGC}^a + \mathcal{L}_{EGC}^b. \quad (37)$$

For regions where the predictions of the two branch networks are consistent, we employ a cross-entropy based cross pseudo-supervision method to impose constraint. Pseudo-labels $\widehat{\mathbf{Y}}_{cnn}^c, \widehat{\mathbf{Y}}_{mamba}^c \in \{0, 1, \dots, K\}^{W \times H}$ are first generated for the consistent predictions of the two branches respectively using argmax function $f_{argmax}(\cdot)$:

$$\widehat{\mathbf{Y}}_{cnn}^c = f_{argmax}(\mathbf{P}_{cnn}^c), \quad (38)$$

$$\widehat{\mathbf{Y}}_{mamba}^c = f_{argmax}(\mathbf{P}_{mamba}^c). \quad (39)$$

Then, the loss for the consistent region is calculated by the cross pseudo-supervision [50] as follows:

$$\mathcal{L}_c = \ell_{ce}(\mathbf{P}_{cnn}^c, \widehat{\mathbf{Y}}_{mamba}^c) + \ell_{ce}(\mathbf{P}_{mamba}^c, \widehat{\mathbf{Y}}_{cnn}^c), \quad (40)$$

where ℓ_{ce} denotes the cross-entropy loss function.

Furthermore, for pixels annotated with scribbles, we employ partial cross-entropy (pCE) supervision on the outputs of both branches, while ignoring unlabeled pixels. And a gated conditional random field (CRF) loss is introduced to mitigate the influence of irrelevant pixels on the classification of the current pixel. This facilitates the model to better perceive morphological information within the input image, thereby emphasizing semantic boundaries. Thereby, the supervised losses calculation for the predictions from the two branch networks are as follows:

$$\mathcal{L}_{sup}^{cnn} = \ell_{pce}(\mathbf{P}_{cnn}, \mathbf{Y}) + \gamma \ell_{crf}(\mathbf{P}_{cnn}), \quad (41)$$

$$\mathcal{L}_{sup}^{mamba} = \ell_{pce}(\mathbf{P}_{mamba}, \mathbf{Y}) + \gamma \ell_{crf}(\mathbf{P}_{mamba}), \quad (42)$$

where ℓ_{pce} represents the partial cross-entropy (pCE) loss function, whose computational formula resembles that of the CE loss function, with the distinction being that N signifies the total number of pixels labeled with scribbles, and pixels in unlabeled regions do not contribute to the calculation. $\mathbf{Y} \in \{0, 1, \dots, K\}^{W \times H}$ represents the labels for scribble annotations, and γ denotes the weight. The computational formula for the gated CRF loss function is as follows:

$$\ell_{crf} = \sum_{i=1}^N \sum_{j=1}^N w_{ij} \cdot \phi(\mathbf{x}_i, \mathbf{x}_j) \cdot (\mathbf{p}_i - \mathbf{p}_j)^2, \quad (43)$$

where N denotes the total number of pixels, w_{ij} represents the gating function to mask unexpected pixel positions, and the function $\phi(\cdot, \cdot)$ serves to quantify the similarity between pixels \mathbf{x}_i and \mathbf{x}_j . Furthermore, \mathbf{p}_i and \mathbf{p}_j represent the predicted probability values for pixels i and j , respectively.

In EDL, due to the utilization of the Dirichlet distribution to represent class probabilities, the direct optimization with the cross-entropy loss function is not feasible. Instead, the optimization target shifts to the expectation of the cross-entropy loss with respect to the Dirichlet distribution. Thereby, we introduce EDL loss function and design the partial EDL (pEDL) loss function to optimize scribble-annotated regions. The calculation of evidence loss is as follows:

$$\mathcal{L}_{evi} = \ell_{pedl}(\mathbf{P}_{cnn}^{evi}, \mathbf{Y}) + \ell_{pedl}(\mathbf{P}_{mamba}^{evi}, \mathbf{Y}), \quad (44)$$

where $\ell_{pedl}(\cdot)$ is the pEDL loss function, which comprises a expected cross-entropy (ECE) loss function and a Kullback-Leibler (KL) loss function:

$$\ell_{pedl} = \frac{f_{sum}[(\ell_{ece} + \varphi \ell_{kl}) \odot \mathcal{M}^s]}{f_{sum}(\mathcal{M}^s)}, \quad (45)$$

$$\varphi = f_{min} \left(1, \frac{2iter}{iter_{max}} \right), \quad (46)$$

where $\ell_{ece}(\cdot)$ is the ECE loss function, ℓ_{kl} is the KL loss function, φ is an annealing coefficient, and $f_{sum}(\cdot)$ denotes summation. By gradually increasing the influence of KL divergence in the loss function through the annealing coefficient φ , the risk of misclassified samples prematurely

converging to a uniform distribution is mitigated. \mathcal{M}^s represents scribble-annotated regions, which are obtained by the following expression:

$$\mathcal{M}^s = 0 \leq \mathbf{Y} \leq K. \quad (47)$$

Note that in this study, classes indexed as K in the labels represent unannotated regions. The ECE essentially optimizes the expectation of cross-entropy under the Dirichlet distribution, necessitating the integration of cross-entropy loss over the Dirichlet distribution. Direct computation of this integral can be challenging, hence, the mean of the Dirichlet distribution is employed as the predicted probability distribution:

$$\begin{aligned} \ell_{ece} &= \int \left[\sum_{k=1}^K -y_i^k \log(p_i^k) \right] D(\mathbf{p}_i | \alpha_i) d\mathbf{p}_i \\ &= \int \left[\sum_{k=1}^K -y_i^k \log(p_i^k) \right] \frac{1}{B(\alpha_i)} \prod_{k=1}^K (p_i^k)^{\alpha_i^k - 1} d\mathbf{p}_i \quad (48) \\ &= \sum_{k=1}^K y_i^k \left[\psi(S_i) - \psi(\alpha_i^k) \right], \end{aligned}$$

where $\psi(\cdot)$ is the *digamma* function. ECE encourages the generation of evidence for positive samples across various classes. Furthermore, to reduce the evidence for negative samples, KL divergence is employed to penalize the generated evidence for negative samples:

$$\begin{aligned} \ell_{kl} &= KL[D(\mathbf{p}_i, \tilde{\alpha}_i) \| D(\mathbf{p}_i, \mathbf{1})] \\ &= \log \left[\frac{\Gamma(\sum_{k=1}^K \tilde{\alpha}_i^k)}{\Gamma(K) \prod_{k=1}^K \Gamma(\tilde{\alpha}_i^k)} \right] \quad (49) \\ &+ \sum_{k=1}^K (\tilde{\alpha}_i^k - 1) \left[\psi(\tilde{\alpha}_i^k) - \psi\left(\sum_{k=1}^K \tilde{\alpha}_i^k\right) \right], \end{aligned}$$

$$\tilde{\alpha}_i = \mathbf{y}_i + (1 - \mathbf{y}_i) \odot \alpha_i, \quad (50)$$

where $\Gamma(\cdot)$ denotes the *gamma* function, $D(\mathbf{p}_i, \mathbf{1})$ is the uniform Dirichlet distribution, $\tilde{\alpha}_i$ represents the Dirichlet parameter after removing misleading evidence from the predictive parameter α_i of sample i . Therefore, the total loss is calculated as follows:

$$\mathcal{L}_{all} = \mathcal{L}_{sup}^{cnn} + \mathcal{L}_{sup}^{mamba} + \mathcal{L}_{evi} + \mathcal{L}_{ic} + \mathcal{L}_c. \quad (51)$$

4. Experiment and results

4.1. Datasets

We validated the proposed method on four common public ultrasound datasets dedicated to segmentation tasks, namely CardiacUDA [16], EchoNet [17], BUSI [18], and DDTI [19], and compared it with alternative approaches. These datasets encompass diverse anatomical regions such as the breast, thyroid, and heart, encompassing both binary and multi-class segmentation tasks.

CardiacUDA: The CardiacUDA dataset, sourced from two anonymous hospitals, includes meticulously collected and annotated cases, approved by 5-6 experienced physicians. Each patient underwent scans in four views: parasternal long-axis left ventricle (LVL), pulmonary artery long-axis (PAL), left ventricular short-axis (LVSA), and apical four-chamber (A4C), producing four videos per patient. Video resolutions range from 800×600 to 1024×768, depending on the scanner (Philips or Hitachi). The dataset comprises approximately 516 and 476 videos from 100 patients per hospital. Each video contains over 100 frames, covering at least one cardiac cycle, with five frames per video annotated at the pixel level for the left ventricle (LV), right ventricle (RV), left atrium (LA), and right atrium (RA).

EchoNet: The EchoNet-Dynamic dataset comprises 10,030 apical four-chamber echocardiography videos sourced from clinical scans conducted at Stanford Hospital between 2016 and 2018. These videos have been preprocessed to exclude non-essential content, resized to 112 × 112 pixels, and annotated with left ventricular endocardial borders at end-systole and end-diastole. We obtained these annotated frames from peers, who shared them online, and we utilized them as segmentation targets to form a new dataset for the image segmentation tasks of this study. This segmentation dataset contains 20,046 images, each accompanied by its corresponding segmentation map.

BUSI: Breast ultrasound images (BUSI) dataset, acquired in 2018, comprises 780 breast ultrasound images from 600 female patients aged 25 to 75, with an average image size of 500×500 pixels. It encompasses ultrasound images of normal, benign, and malignant breast cancer cases, along with their corresponding segmentation maps.

Table 1: Quantitative comparison results on the CardiacUDA dataset. The U-Net is trained with full supervision, serving as an upper bound. The results in bold are the best, and those in italics are the second best.

Metrics	Methods	Left ventricle	Left atrium	Right atrium	Right ventricle	Mean
Dice (%) \uparrow	U-Net [5] (dense label) (upper bound)	76.49 \pm 0.71	76.47 \pm 1.08	79.26 \pm 0.78	76.23 \pm 0.47	77.11 \pm 1.47
	U-Net + pCE [51] (lower bound)	69.28 \pm 0.87	51.50 \pm 3.35	67.42 \pm 2.18	70.83 \pm 0.82	64.76 \pm 8.18
	U-Net + USTM [42]	68.89 \pm 1.16	52.53 \pm 0.81	67.83 \pm 1.58	70.03 \pm 0.97	64.82 \pm 7.40
	U-Net + Gated CRF [37]	<i>73.10 \pm 1.04</i>	<i>74.06 \pm 1.46</i>	<i>77.63 \pm 1.19</i>	<i>73.67 \pm 0.75</i>	<i>74.62 \pm 2.03</i>
	DMPLS [9]	66.61 \pm 0.13	57.09 \pm 1.45	71.59 \pm 1.85	69.12 \pm 1.81	66.10 \pm 5.80
	ScribbleVC [39]	70.82 \pm 0.87	69.36 \pm 1.64	73.85 \pm 0.49	71.79 \pm 0.77	71.45 \pm 1.92
	ScribFromer [40]	62.56 \pm 2.67	54.84 \pm 2.13	66.76 \pm 1.34	63.44 \pm 2.85	61.90 \pm 4.96
	Ours	74.36 \pm 0.44	75.16 \pm 1.07	77.85 \pm 0.77	74.19 \pm 0.79	75.39 \pm 1.67
95HD (pixel) \downarrow	U-Net [5] (dense label) (upper bound)	16.25 \pm 0.69	8.94 \pm 0.92	6.43 \pm 0.28	7.59 \pm 0.43	9.80 \pm 3.97
	U-Net + pCE [51] (lower bound)	25.03 \pm 2.25	80.88 \pm 5.41	28.82 \pm 7.61	15.63 \pm 0.49	37.59 \pm 26.48
	U-Net + USTM [42]	27.08 \pm 2.39	76.57 \pm 2.63	37.64 \pm 11.68	13.66 \pm 1.27	38.74 \pm 24.70
	U-Net + Gated CRF [37]	<i>18.72 \pm 0.58</i>	<i>11.43 \pm 1.34</i>	<i>7.68 \pm 0.35</i>	<i>9.84 \pm 0.24</i>	<i>11.92 \pm 4.43</i>
	DMPLS [9]	26.65 \pm 0.66	59.85 \pm 2.52	14.79 \pm 2.46	13.86 \pm 0.75	28.79 \pm 19.19
	ScribbleVC [39]	20.19 \pm 0.56	15.12 \pm 1.41	10.98 \pm 0.60	10.29 \pm 0.26	14.14 \pm 4.12
	ScribFromer [40]	32.74 \pm 5.09	38.68 \pm 14.59	24.34 \pm 6.65	21.86 \pm 2.53	29.41 \pm 10.40
	Ours	18.57 \pm 0.39	10.56 \pm 1.41	7.64 \pm 0.37	9.64 \pm 0.12	11.60 \pm 4.33

DDTI: The digital database of thyroid ultrasound images (DDTI), an open resource for the scientific community, supported by Universidad Nacional de Colombia, CIM@LAB, and Instituto de Diagnostico Medico (IDIME), encompasses 99 cases, 134 images, covering thyroiditis, cystic nodules, adenomas, and cancer. Our study utilized a preprocessed version provided by the authors of the first-place solution in the MICCAI 2020 TN-SCUI Challenge, who cleansed, cropped, and removed irrelevant regions.

4.2. Implementation details and evaluation metrics

For this study, images sourced from BUSI and DDTI were resized to 256×256 pixels for uniformity. For the BUSI dataset, we exclusively utilized samples with lesions and segmentation masks, discarding normal samples without segmentation targets. Furthermore, for samples

with multiple lesion areas, the segmentation masks were merged. For the EchoNet dataset, we utilized the original size, i.e., 112×112 pixels. Moreover, annotated frames from CardiacUDA were extracted and resized to the same 256×256 pixel resolution, creating a new segmentation dataset comprising 2,250 images. All scribble annotations were generated by the WSL4MIS code² provided by HiLab at UESTC. This method initially extracts the two largest connected components from a binary mask. It then detects and processes branching structures in the image, removing unnecessary branches. Finally, it generates a skeletonization representation of the 2D image, which is used to create doodles. In the generated annotations, the background class is represented as 0, and the unlabeled

²<https://github.com/HiLab-git/WSL4MIS>

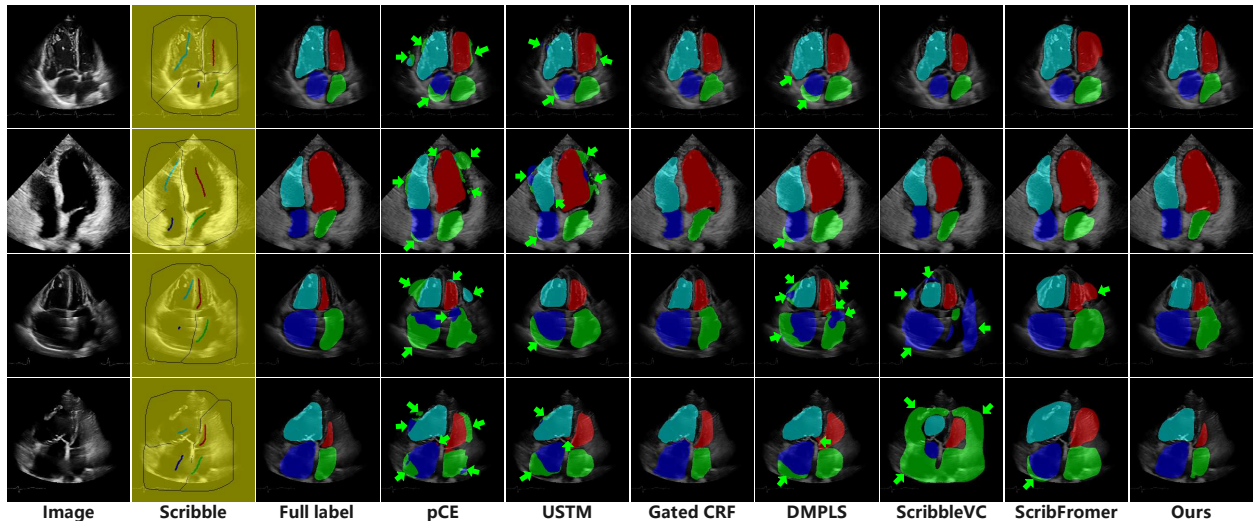


Figure 4: Visualization of experimental results comparison on the CardiacUDA dataset. The *Scribble* column represents scribble annotations, while the *Full label* column indicates full dense annotations. Green arrows point out the missegmented regions.

class is denoted as K (i.e., the largest number excluding other categories). The scribble annotations we generated are relatively sparse. We evaluated the proposed method and other methods on all datasets using five-fold cross-validation. The optimizer used to train the model is Stochastic Gradient Descent (SGD), with a weight decay of 10^{-4} and a momentum of 0.9, to minimize the joint objective function Eq. 51. We implemented our proposed method and other comparison methods based on Python 3.8, PyTorch 1.12, and the WSL4MIS codebase², and trained them on a server with 2 Nvidia Geforce RTX 3080 GPUs, totaling 20GB of memory. Images were pre-processed before training, including random horizontal or vertical flipping, random angle rotation, random equalization, and random adjustments of brightness, contrast, saturation, and hue. The learning rate was adjusted online by the poly learning rate scheduler [9]:

$$LR_{iter} = \left(1.0 - \frac{iter}{iter_{max}}\right)^{0.9} LR_0, \quad (52)$$

where LR_{iter} denotes the learning rate at the $iter$ -th iteration. The batch size and total iterations ($iter$) were set to 12 and 60k, respectively. Hyper-parameters τ , ϵ and γ were set to 0.25, 0.5 and 0.1, respectively. For a **fair** comparison, we employed the output of U-Net as the fi-

nal result in the testing phase without applying any post-processing methods. And all experiments were conducted in the same experimental environment.

We quantitatively evaluated all methods using 4 metrics widely adopted in weakly or semi-supervised medical image segmentation tasks. The evaluation metrics encompass the Dice score, Jaccard index, average surface distance (ASD), and 95% Hausdorff distance (95HD). The Dice score and Jaccard index assess pixel-level overlap between the ground truth and predictions, while ASD and 95HD measure the surface distances between them. **Note** that for the multi-class segmentation task on the CardiacUDA dataset, we only present Dice and 95HD as evaluation metrics.

4.3. Comparison with existing methods

This subsection compared our proposed MambaEviScrib with 5 advanced scribble-supervised learning methods on 4 diverse datasets. The methods encompass pCE [51], USTM [42], Gated CRF [37], DMPLS [9], ScribbleVC [39], and ScribFromer [40]. pCE, serving as the baseline, set the lower bound for all approaches. The backbone of pCE, USTM, and Gated CRF is the U-Net architecture, while both ScribbleVC and ScribFromer incorporate Transformers. Additionally, a fully supervised

Table 2: Quantitative comparison results on the EchoNet dataset. The U-Net is trained with full supervision, serving as an upper bound. The results in bold are the best, and those in italics are the second best.

Methods	Dice (%) \uparrow	Jaccard (%) \uparrow	95HD (pixel) \downarrow	ASD (pixel) \downarrow
U-Net [5] (upper bound)	92.64 \pm 0.08	86.57 \pm 0.10	2.79 \pm 0.06	1.12 \pm 0.02
U-Net + pCE [51] (lower bound)	68.57 \pm 0.81	53.53 \pm 0.97	12.38 \pm 0.68	6.38 \pm 0.17
U-Net + USTM [42]	71.60 \pm 3.57	57.19 \pm 4.19	12.35 \pm 1.48	5.51 \pm 1.06
U-Net + Gated CRF [37]	84.31 \pm 0.59	73.60 \pm 0.84	6.14 \pm 0.23	2.58 \pm 0.13
DMPLS [9]	74.52 \pm 1.05	60.54 \pm 1.41	10.30 \pm 0.63	4.00 \pm 0.52
ScribbleVC [39]	84.77 \pm 0.58	74.19 \pm 0.82	6.01 \pm 0.18	2.43 \pm 0.10
ScribFormer [40]	63.53 \pm 1.71	47.69 \pm 1.74	15.48 \pm 0.70	7.90 \pm 0.58
Ours	85.10 \pm 0.52	74.78 \pm 0.73	5.95 \pm 0.24	2.38 \pm 0.11

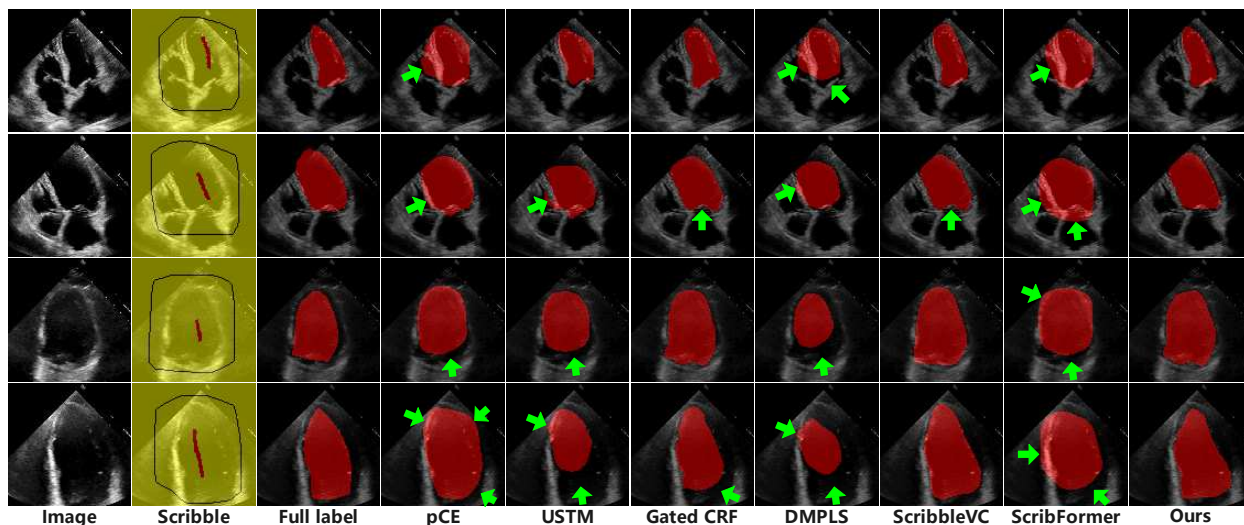


Figure 5: Visualization of comparison experimental results on the EchoNet dataset. The *Scribble* column represents scribble annotations, while the *Full label* column indicates full dense annotations. Green arrows point out the missegmented regions.

U-Net [5] was trained to serve as an upper reference. It is **noteworthy** that while our method incorporated U-Net and Mamba-UNet, only U-Net was required during testing or inference.

4.3.1. Results on the CardiacUDA dataset

The quantitative results of all methods obtained from the experiments on the challenging CardiacUDA dataset are presented in Table 1. As can be seen from the table, The baseline method, pCE, performed mediocly and served as a benchmark for scribble-supervised segmen-

tation performance. The performance of all other methods surpassed that of pCE. Among the existing methods, Gated CRF exhibited commendable performance, ranking second only to the proposed approach, with the mean Dice score of 74.62% and the 95HD of 11.74. This suggested that Gated CRF holds an advantage in the task of scribble-supervised segmentation on ultrasound datasets, attributed to its capability of perceiving morphological features of anatomical structures. Our proposed method achieved the highest performance on all evaluation metrics for the scribble-supervised task on this dataset, with

Table 3: Quantitative comparison results on the BUSI dataset. The U-Net is trained with full supervision, serving as an upper bound. The results in bold are the best, and those in italics are the second best.

Methods	Dice (%) \uparrow	Jaccard (%) \uparrow	95HD (pixel) \downarrow	ASD (pixel) \downarrow
U-Net [5] (upper bound)	77.91 \pm 2.54	69.52 \pm 2.45	29.75 \pm 3.86	11.18 \pm 1.76
U-Net + pCE [51] (lower bound)	62.89 \pm 2.90	50.36 \pm 3.39	47.03 \pm 5.77	18.96 \pm 2.27
U-Net + USTM [42]	61.99 \pm 3.05	49.11 \pm 3.05	47.50 \pm 5.16	19.20 \pm 2.41
U-Net + Gated CRF [37]	<i>71.39 \pm 2.66</i>	<i>60.84 \pm 2.37</i>	35.90 \pm 2.86	13.54 \pm 1.49
DMPLS [9]	65.09 \pm 3.44	52.85 \pm 3.45	36.27 \pm 3.21	14.63 \pm 1.58
ScribbleVC [39]	69.92 \pm 3.87	57.90 \pm 3.90	<i>31.23 \pm 5.67</i>	<i>12.55 \pm 2.85</i>
ScribFromer [40]	65.09 \pm 3.44	52.85 \pm 3.45	36.27 \pm 3.21	14.63 \pm 1.58
Ours	74.07 \pm 3.27	63.99 \pm 3.18	31.10 \pm 2.73	11.71 \pm 1.60

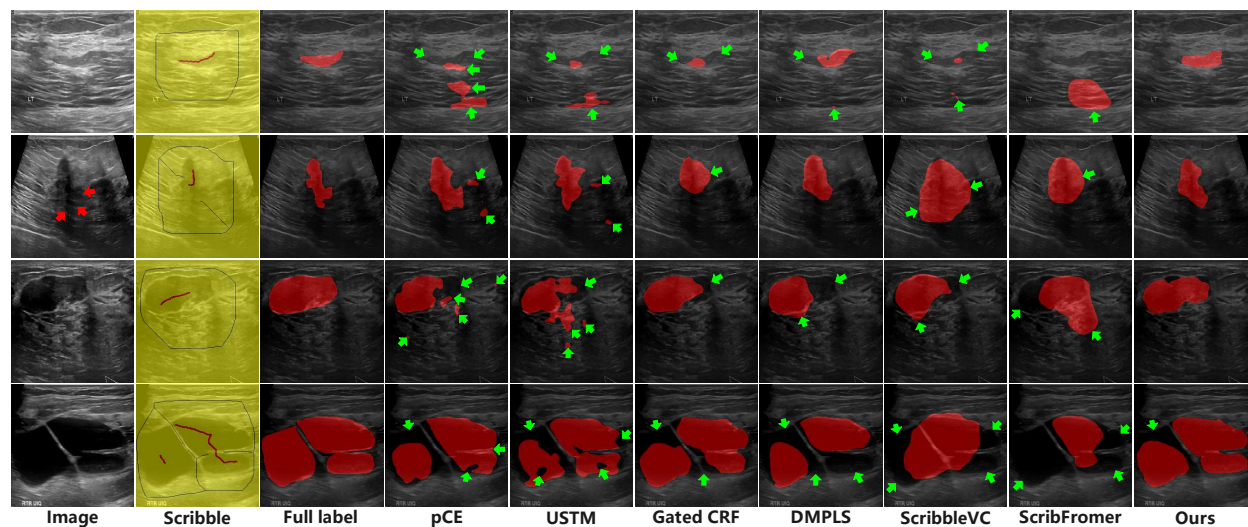


Figure 6: Visualization of comparison experimental results on the BUSI dataset. The *Scribble* column represents scribble annotations, while the *Full label* column indicates full dense annotations. Green arrows point out the missegmented regions, and red arrows point to the indistinguishable boundaries.

the mean Dice score of 74.62% and the 95HD of 11.74, outperforming Gated CRF by 0.77% in Dice score. This may stem from the model’s tendency to prioritize learning easily segmentable classes, thereby introducing unfairness. In contrast, our method not only achieved overall superior segmentation performance but also demonstrated a narrower performance gap among different classes, highlighting its superiority and robustness.

We visualized the segmentation results as shown in Fig. 4, aiming to provide a clear and intuitive understand-

ing of the performance differences between various methods. The green arrows in the figure pointed out the regions where segmentation errors occurred. As seen from the figure, the images in the first and second rows exhibited higher quality and clearer boundaries compared to those in the third and fourth rows, resulting in overall better segmentation outcomes. Most segmentation methods committed errors in segmenting the images in the third and fourth rows, whereas our method avoided the severe mistake of misidentifying anatomical structural lo-

Table 4: Quantitative comparison results on the DDTI dataset. The U-Net is trained with full supervision, serving as an upper bound. The results in bold are the best, and those in italics are the second best.

Methods	Dice (%) \uparrow	Jaccard (%) \uparrow	95HD (pixel) \downarrow	ASD (pixel) \downarrow
U-Net [5] (upper bound)	79.23 ± 1.74	68.57 ± 1.66	27.03 ± 1.69	10.15 ± 0.85
U-Net + pCE [51] (lower bound)	64.27 ± 1.53	50.22 ± 1.45	39.53 ± 1.89	19.00 ± 1.14
U-Net + USTM [42]	63.86 ± 1.66	49.65 ± 1.58	39.61 ± 2.15	19.08 ± 1.47
U-Net + Gated CRF [37]	66.53 ± 1.02	52.48 ± 1.12	35.58 ± 0.96	16.12 ± 0.69
DMPLS [9]	62.88 ± 1.59	48.71 ± 1.54	41.12 ± 2.41	19.85 ± 1.38
ScribbleVC [39]	62.50 ± 1.61	47.93 ± 1.69	39.89 ± 2.78	19.32 ± 1.52
ScribFromer [40]	59.68 ± 1.95	45.08 ± 1.93	43.15 ± 2.53	21.50 ± 1.41
Ours	68.04 ± 3.58	54.18 ± 4.05	34.69 ± 3.67	14.79 ± 2.56

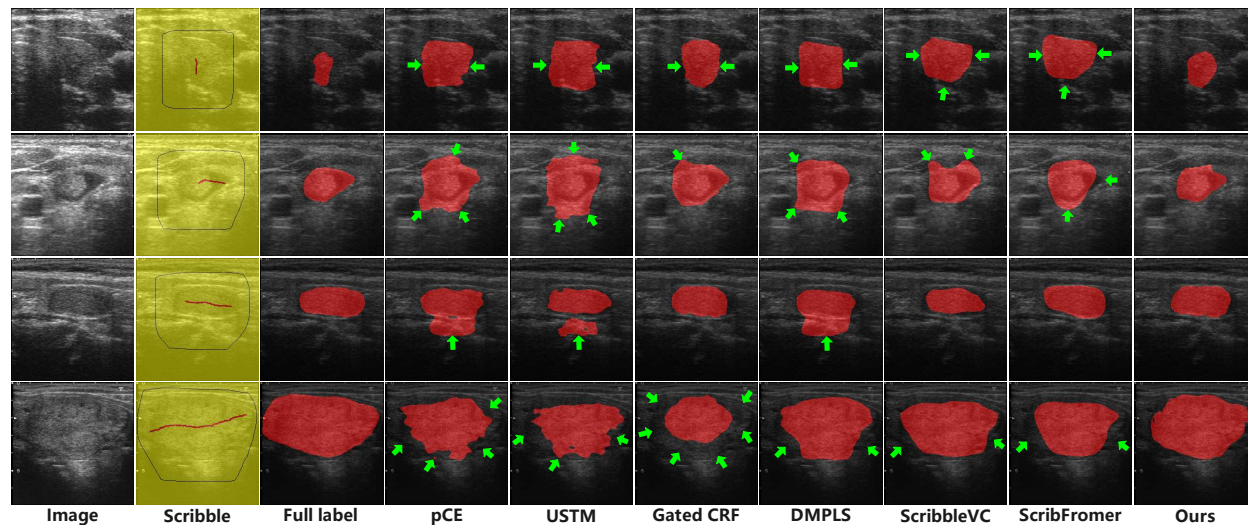


Figure 7: Visualization of comparison experimental results on the DDTI dataset. The *Scribble* column represents scribble annotations, while the *Full label* column indicates full dense annotations. Green arrows point out the missegmented regions.

cations. In relative terms, pCE, USTM, and DMPLS exhibited a higher number of segmentation error regions. From the figure, we observed that the most prevalent error was the misidentification of other cardiac chambers as the left atrium, likely attributed to the small proportion of the left atrium’s area in most echocardiographic images, rendering it challenging for weakly supervised models to adequately capture the characteristics of the left atrium. Furthermore, our observations revealed that ScribbleVC tended to adopt a conservative approach in segmenting certain regions, such as the left and right ventricles in the

figure, failing to fully delineate the target objects. Conversely, it exhibited a more aggressive segmentation in other regions, like the left and right atria in the figure, by erroneously including substantial non-target areas within the segmentation. While it has been reported to excel in magnetic resonance image segmentation in the literature [39], it may not be adaptable to the segmentation of ultrasound images.

In summary, our MambaEviSrib demonstrated promising performance in the multi-class segmentation of echocardiography, featuring a reduction in critical errors

Table 5: Ablation experiment results of the dual-branch network on the BUSI dataset. The results in bold are the best. FLOPs represent the floating point operations of the Branch-2 model, and Time indicates the duration it takes for the Branch-2 model to input and process a single image.

Branch-1	Branch-2	Dice (%) \uparrow	95HD (pixel) \downarrow	Params (M) \downarrow	FLOPs (G) \downarrow	Time (ms) \downarrow
U-Net	HRNet	72.92 \pm 3.57	35.23 \pm 4.80	9.64	4.65	38.33 \pm 0.33
U-Net	TransUNet	73.22 \pm 3.40	33.67 \pm 4.29	105.32	33.41	16.33 \pm 0.43
U-Net	Swin-UNet	72.52 \pm 3.84	32.91 \pm 5.41	41.39	11.37	15.72 \pm 0.51
U-Net	Mamba-UNet	74.07 \pm 3.27	31.80 \pm 2.73	19.12	4.56	9.59 \pm 0.14

Table 6: Ablation experiment results of the dual-branch network on the CardiacUDA dataset. The results in bold are the best.

Metrics	Branch-1	Branch-2	Left ventricle	Left atrium	Right atrium	Right ventricle	Mean
Dice (%) \uparrow	U-Net	HRNet	73.68 \pm 1.42	74.10 \pm 0.90	76.94 \pm 0.54	73.95 \pm 0.53	74.67 \pm 1.59
	U-Net	TransUNet	74.03 \pm 0.81	73.72 \pm 0.42	76.77 \pm 0.60	73.83 \pm 0.48	74.59 \pm 1.41
	U-Net	Swin-UNet	73.97 \pm 0.14	73.73 \pm 0.74	77.27 \pm 0.47	73.31 \pm 0.51	74.57 \pm 1.70
	U-Net	Mamba-UNet	74.36 \pm 0.44	75.16 \pm 1.07	77.85 \pm 0.77	74.19 \pm 0.79	75.39 \pm 1.67
95HD (pixel) \downarrow	U-Net	HRNet	18.67 \pm 0.13	10.90 \pm 0.95	7.63 \pm 0.54	9.48 \pm 0.33	11.67 \pm 4.42
	U-Net	TransUNet	18.63 \pm 0.13	11.07 \pm 1.37	7.89 \pm 0.50	9.71 \pm 0.29	11.83 \pm 4.31
	U-Net	Swin-UNet	19.50 \pm 0.98	10.72 \pm 0.81	7.56 \pm 0.44	10.32 \pm 0.72	12.03 \pm 4.73
	U-Net	Mamba-UNet	18.57 \pm 0.39	10.56 \pm 1.41	7.64 \pm 0.37	9.64 \pm 0.12	11.60 \pm 4.33

and generally improved segmentation accuracy. Moreover, our method depicted edge details more accurately, indicating its perception of global morphological characteristics.

4.3.2. Results on the EchoNet dataset

We further conducted a comparison experiment on another echocardiography dataset EchoNet, and the quantitative results are shown in Table 2. The pCE remained as the baseline method. Surprisingly, however, ScribbleFormer performed poorly on this dataset, even falling below the lower bound. This is likely attributed to the limited annotation information, which prevented it from accurately capturing the characteristics of segmentation objects, such as morphology and edges. The majority of the remaining methods surpassed the baseline approach, with ScribbleVC achieving good performance, ranking second only to our method, with Dice scores and 95HD of 84.77% and 6.01 respectively. In contrast to its performance on the CardiacUDA dataset, on this dataset, ScribbleVC surpassed the Gated CRF method, relegating the

latter to third place. Our method demonstrated optimal performance, achieving 85.10% Dice and 5.95 in 95HD, respectively. While there existed a gap compared to fully supervised methods, it is important to note that this was achieved under the premise of extremely sparse scribble annotations, which constituted a minimal fraction of the segmented objects, posing significant challenges. Furthermore, confronted with the challenge of varying left ventricular shapes in the EchoNet dataset, our method exhibited satisfactory performance, indicating its capability to capture global information and morphological features.

All segmentation results are visualized in Fig. 5. Four echocardiographic images of the left ventricle with varying sizes were selected, and arranged from top to bottom in ascending order of scale. The green arrows in the figure pointed out the regions where segmentation errors were apparent. As can be seen from the figure, some methods tended to be aggressive in segmentation, especially when dealing with small left ventricles. In the case of large-sized left ventricles, methods like USTM and DM-PLS displayed a pronounced tendency towards conserva-

Table 7: Ablation experiment results of the consistency strategy on the BUSI dataset. EDL stands for evidential deep learning, while EGC represents evidence-guided consistency strategy. The results in bold are the best.

EDL	EGC	Dice (%) \uparrow	Jaccard (%) \uparrow	95HD (pixel) \downarrow	ASD (pixel) \downarrow
		72.72 \pm 3.35	61.99 \pm 3.30	32.73 \pm 5.02	12.24 \pm 2.61
\checkmark		73.59 \pm 2.76	63.28 \pm 2.82	33.41 \pm 7.21	11.72 \pm 2.99
\checkmark	\checkmark	74.07 \pm 3.27	63.99 \pm 3.18	31.10 \pm 2.73	11.71 \pm 1.60

Table 8: Ablation experiment results of the consistency strategy on the CardiacUDA dataset. EDL stands for evidential deep learning, while EGC represents evidence-guided consistency strategy. The results in bold are the best.

Metrics	EDL	EGC	Left ventricle	Left atrium	Right atrium	Right ventricle	Mean
Dice (%) \uparrow			74.31 \pm 0.23	73.69 \pm 1.47	76.44 \pm 0.83	71.16 \pm 0.59	73.90 \pm 2.11
	\checkmark		74.05 \pm 0.31	73.46 \pm 1.24	77.10 \pm 0.40	74.06 \pm 0.83	74.67 \pm 1.63
	\checkmark	\checkmark	74.36 \pm 0.44	75.16 \pm 1.07	77.85 \pm 0.77	74.19 \pm 0.79	75.39 \pm 1.67
95HD (pixel) \downarrow			18.39 \pm 0.26	10.85 \pm 1.25	8.48 \pm 1.04	15.94 \pm 0.15	13.42 \pm 4.17
	\checkmark		18.82 \pm 0.30	10.86 \pm 0.67	7.86 \pm 0.32	9.56 \pm 0.35	11.77 \pm 4.41
	\checkmark	\checkmark	18.57 \pm 0.39	10.56 \pm 1.41	7.64 \pm 0.37	9.64 \pm 0.12	11.60 \pm 4.33

tive segmentation, significantly compromising the precision of the anatomical delineation achieved. This suggests that these methods had an insufficient capture of global information. Among the two methods, ScribFormer’s segmented regions notably exhibited a tendency towards aggressiveness in comparison to DMPLS, which we hypothesize may stem from the influence of the Transformer architecture. Nonetheless, they remained insufficient in adequately capturing the morphological characteristics. Furthermore, we notice that some methods failed to segment the region covered by the mitral valve, excluding it from the left ventricle. We speculate that this could be due to the insufficient coverage of scribble annotations in this region, resulting in the model’s inability to capture its features. In summary, our method can overcome most of the above problems and demonstrate advantages in ultrasonic data.

4.3.3. Results on the BUSI dataset

In addition to echocardiography data, we also conducted comparison experiments on the breast ultrasound dataset BUSI, with the results presented in Table 3. Among the existing approaches, the Gated CRF method

continued to exhibit the best performance, achieving a Dice score of 71.39%, significantly outperforming the baseline method pCE. Our proposed method, however, surpassed the Gated CRF by a notable margin, attaining a Dice score of 74.62%, which represented a 3.23% improvement over Gated CRF and further narrowed the gap towards the fully supervised upper bound of 77.91%. Our method exhibited the most significant improvement on this dataset among the four, indicating a certain advantage in breast lesion detection.

All segmentation results are visualized in Fig. 6. We selected a representative set of images and their corresponding segmentation outcomes, encompassing lesions of varying morphologies and sizes, for presentation. The lesions in the first row of images were relatively small, posing challenges for some methods that tended to falsely segment similar regions as lesions, leading to false positives, while others may fail to fully segment the lesions, resulting in false negatives. The lower boundary of the lesion in the second row of images is indistinct (as indicated by the red arrow), posing difficulties even for human eyes to discern, thereby hindering some methods from accu-

rately segmenting the boundary. The lesion in the fourth row of images comprises multiple adjacent lesions, a relatively rare occurrence in the dataset. Consequently, most methods struggled to accurately capture its morphological characteristics. Furthermore, the large size of this lesion necessitates a model’s ability to comprehend global information. While our approach did not achieve perfection, it outperformed existing methods. Additionally, from the visualization results, it is evident that the pCE and USTM methods segmented a relatively higher number of false positive lesions in some images of this dataset, which is inferior to our approach.

4.3.4. Results on the DDTI dataset

We also conducted experiments on another challenging dataset, DDTI, for thyroid nodule ultrasound image segmentation, with the results presented in Table 4. On this dataset, the Gated CRF method continued to maintain the best performance among the existing methods, whereas the USTM method, unfortunately, once again fell below the lower bound. Our method continued to outperform others, achieving a Dice score of 68.04%, which is a 1.51% improvement over the Gated CRF method. However, it was regrettable that there was still a certain gap from the upper bound, which was attributed to the significant challenges posed by this dataset for weak supervision.

All segmentation results are visualized in Fig. 7, with the selected lesions arranged from small to large in size. Some methods tended to produce false positives for small-sized lesions and false negatives for large-sized lesions. Overall, our method exhibited better performance compared to existing methods. However, upon observing the ultrasound images from the four visualization examples, it becomes evident that the lesion boundaries are unclear, making it difficult to distinguish between the lesions and normal tissues. This poses a significant challenge for weakly supervised segmentation and underscores the need for continued focus and improvement in this area of ultrasound image segmentation in the future.

4.4. Ablation study

4.4.1. Comparison of the dual-branch network

To demonstrate the superiority of Mamba-UNet within the Mamba branch of our proposed method, we conducted experiments by replacing it with other advanced

networks. These networks include the Swin-UNet and TransUNet, both of which leverage the Transformer architecture, as well as the purely CNN-based HRNet. We compared their performance and efficiency on the BUSI and CardiacUDA datasets. For fairness, only U-Net was utilized for inference during the testing phase. The experimental results, presented in Tables 5 and 6, demonstrated that our method achieved the optimal performance with the second-least number of parameters, trailing only HRNet. However, in terms of floating-point operations (FLOPs), our method surpassed even the CNN-based HRNet, recording the lowest FLOPs at 4.56G. Furthermore, our method operated at the fastest speed, taking approximately 9.59ms to process and segment an input image of 256×256 pixels, which is 1.64 times faster than the second-fastest, Swin-UNet. This underscored the capability of the Mamba model to significantly reduce computational complexity while effectively capturing long-range dependencies.

4.4.2. Comparison of the consistency strategy

To validate the effectiveness of EDL and EGC, ablation experiments were conducted on the BUSI and CardiacUDA datasets, with the experimental results presented in Tables 7 and 8. Given that EGC relies on EDL, we initially removed EGC from the framework and replaced it with a conventional mean squared error (MSE) constraint to validate the superiority of EGC. According to the experimental results, our complete method outperformed the conditions where either EGC or both EGC and EDL were removed. Specifically, compared to the condition where both EGC and EDL were removed, our complete method achieved a 1.32% higher Dice score on the BUSI dataset and a 1.49% higher Dice score on the CardiacUDA dataset. In summary, the proposed EGC exhibited certain advantages, facilitating the model’s ability to better handle pixels located at decision boundaries, such as blurred edges in ultrasound images, thereby enhancing performance.

4.4.3. Hyper-parameter analysis

We conducted an analysis on 3 hyper-parameters that require manual tuning, namely τ , ϵ , and γ . The parameter τ served as a scaling factor in the transformation function $f_e(\cdot)$ (see Eq. 10), modulating the smoothness of the function. ϵ , as the sharpening temperature in Eqs. 30 and 34,

Table 9: Generalization evaluation of models. The models trained on the CardiacUDA dataset are tested on the EchoNet dataset.

Methods	Dice (%) \uparrow	Jaccard (%) \uparrow	95HD (pixel) \downarrow	ASD (pixel) \downarrow
U-Net + pCE	66.76 \pm 6.65	53.57 \pm 6.59	13.01 \pm 1.95	4.31 \pm 0.54
U-Net + USTM	63.08 \pm 7.69	49.89 \pm 7.60	13.95 \pm 1.25	4.57 \pm 0.18
U-Net + Gated CRF	74.13 \pm 0.61	61.87 \pm 0.49	11.14 \pm 0.34	3.26 \pm 0.21
DMPLS	60.07 \pm 3.31	46.93 \pm 2.88	15.33 \pm 0.84	4.59 \pm 0.17
ScribbleVC	64.87 \pm 1.95	51.99 \pm 1.96	13.80 \pm 0.66	3.75 \pm 0.30
ScribFromer	66.35 \pm 4.09	52.69 \pm 4.49	15.28 \pm 1.34	5.36 \pm 0.77
Ours	76.39 \pm 1.64	64.22 \pm 1.66	10.82 \pm 0.54	3.37 \pm 0.10

biases predictions of high evidence towards regions of higher density. The parameter γ in Eqs. 41 and 42 served as a balancing weight between the loss functions pCE and Gated CRF. According to the experiments, the model achieved optimal performance when τ , ϵ , and γ were set to 0.25, 0.5, and 0.1 respectively. In summary, variations in the settings of these hyperparameters exerted a certain influence on the model’s performance, with ϵ having the least impact, resulting in a maximum Dice difference of merely 0.44%, whereas γ exerted a more significant influence, leading to a maximum Dice difference of 1.37%. This disparity could potentially be attributed to the influential nature of the Gated CRF loss.

4.5. Generalization and robustness analysis

4.5.1. Generalization analysis

To assess the generalization capabilities of each model, we subjected the models trained on the CardiacUDA dataset to testing on the EchoNet dataset, which served as an out-of-distribution (OOD) dataset. This is crucial when applying the models in real-world clinical scenarios. As the EchoNet dataset is dedicated solely to segmenting the left ventricle, whereas the CardiacUDA dataset encompassed all four cardiac chambers including the left ventricle, only the left ventricular segmentation results were retained during testing on the EchoNet dataset. Furthermore, given that the images in the CardiacUDA dataset are of size 256 \times 256 pixels, whereas those in the EchoNet dataset are 112 \times 112 pixels, all images were first upsampled to 256 \times 256 pixels before testing on the EchoNet dataset. Subsequently, the obtained prediction masks were downsampled to 112 \times 112 pixels, upon which the evaluation metrics were calculated. The evaluation results are presented

in Table 9. The findings indicate that among the existing methods, the Gated CRF method performed the best, while the other existing methods even underperformed the baseline pCE method, suggesting their inadequate generalization capabilities and possible overfitting issues. In contrast, the proposed method outperformed all others, achieving a 2.26% higher Dice score than the second-best Gated CRF method, demonstrating its superior generalization ability. This is because the theory of evidence provides a solid mathematical foundation for EDL, enabling the model to accurately quantify prediction uncertainty. The evidence loss function directed the model to minimize prediction errors while also minimizing the under- or overestimation of uncertainty. This robust learning process facilitated the model’s ability to learn more generalized feature representations, rather than merely memorizing noise or specific patterns within the training data.

4.5.2. Robustness analysis

When applying models in real-world clinical scenarios, they sometimes need to confront noisy data. Therefore, it is necessary to test the performance of the model on noisy data to validate its robustness. We applied Gaussian noise to degrade the image quality on both the BUSI dataset and the CardiacUDA dataset, simulating scenarios of low-quality data acquisition. We considered three distinct levels of Gaussian noise, characterized by standard deviations σ of 0.05, 0.1, and 0.15, respectively, under the condition that image pixels had been normalized to a range of 0 to 1. As evident from the experimental results presented in Tables 10 and 11, when $\sigma = 0.05$, the performance degradation observed for all methods was relatively small, whereas our method maintained optimal per-

Table 10: Evaluation of model robustness on the BUSI Dataset. The symbol σ represents the standard deviation of the Gaussian noise added to the image.

Methods	Dice (%) \uparrow	95HD (pixel) \downarrow	Dice (%) \uparrow	95HD (pixel) \downarrow
	No noise		$\sigma = 0.05$	
U-Net + pCE	62.89 \pm 2.90	47.03 \pm 5.77	60.32 \pm 3.85 ^{-2.57}	49.41 \pm 3.67
U-Net + USTM	61.99 \pm 3.05	47.50 \pm 5.16	60.41 \pm 3.83 ^{-1.58}	46.42 \pm 4.96
U-Net + Gated CRF	71.39 \pm 2.66	35.90 \pm 2.86	69.71 \pm 2.73 ^{-1.69}	37.85 \pm 1.99
DMPLS	65.09 \pm 3.44	36.27 \pm 3.21	62.80 \pm 3.91 ^{-2.30}	36.82 \pm 6.49
ScribbleVC	69.92 \pm 3.87	31.23 \pm 5.67	67.84 \pm 3.30 ^{-2.08}	34.24 \pm 3.56
ScribFromer	65.09 \pm 3.44	36.27 \pm 3.21	55.51 \pm 3.09 ^{-9.58}	45.53 \pm 2.10
Ours	74.07 \pm 3.27	31.10 \pm 2.73	72.92 \pm 3.99^{-1.15}	30.38 \pm 2.47
	$\sigma = 0.10$		$\sigma = 0.15$	
U-Net + pCE	52.58 \pm 4.15 ^{-10.31}	55.96 \pm 8.79	38.71 \pm 9.08 ^{-24.18}	66.86 \pm 14.73
U-Net + USTM	50.63 \pm 5.89 ^{-11.35}	45.19 \pm 8.31	31.89 \pm 14.46 ^{-30.10}	47.87 \pm 15.54
U-Net + Gated CRF	62.23 \pm 4.26 ^{-9.16}	41.58 \pm 5.98	48.60 \pm 10.58 ^{-22.79}	41.87 \pm 7.13
DMPLS	45.96 \pm 5.88 ^{-19.13}	54.66 \pm 23.12	22.20 \pm 6.39 ^{-42.89}	55.01 \pm 27.41
ScribbleVC	53.40 \pm 10.40 ^{-16.52}	56.38 \pm 17.52	35.21 \pm 7.48 ^{-34.71}	87.06 \pm 16.43
ScribFromer	54.69 \pm 3.64 ^{-10.41}	46.02 \pm 1.84	43.35 \pm 10.79 ^{-21.74}	64.86 \pm 25.09
Ours	65.54 \pm 3.76^{-8.53}	39.21 \pm 4.22	55.11 \pm 2.40^{-18.97}	51.55 \pm 14.14

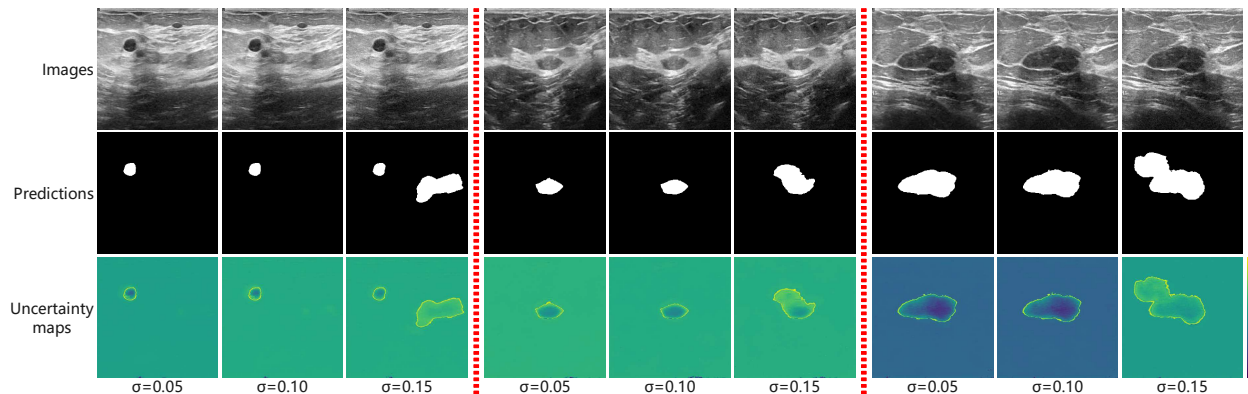


Figure 8: Visualization of the uncertainty map for the test results of our model on the BUSI dataset. The symbol σ represents the standard deviation of the Gaussian noise added to the image.

formance with the least degradation, demonstrated by a mere 0.31% decrease in Dice score on the CardiacUDA dataset. When theta increased to 0.1, our method remained optimal with minimal performance degradation. However, under extreme conditions where theta reaches 0.15, while most methods experienced significant per-

formance deterioration, our method still retained an advantage, demonstrating the best performance with the least degradation. Specifically, on the BUSI dataset, our method outperformed the worst-performing DMPLS Dice by a significant margin of 32.91%, demonstrating a substantial advantage. On the CardiacUDA dataset, our per-

Table 11: Evaluation of model robustness on the CardiacUDA Dataset. The symbol σ represents the standard deviation of the Gaussian noise added to the image.

Methods	Dice (%) \uparrow	95HD (pixel) \downarrow	Dice (%) \uparrow	95HD (pixel) \downarrow
	No noise		$\sigma = 0.05$	
U-Net + pCE	64.76 \pm 8.18	37.59 \pm 26.48	64.39 \pm 1.22 ^{-0.37}	31.50 \pm 0.92
U-Net + USTM	64.82 \pm 7.40	38.74 \pm 24.70	63.67 \pm 1.94 ^{-1.15}	35.05 \pm 1.06
U-Net + Gated CRF	74.87 \pm 2.03	11.72 \pm 4.43	74.18 \pm 0.49 ^{-0.69}	12.61 \pm 0.93
DMPLS	66.10 \pm 5.80	28.79 \pm 19.19	65.68 \pm 0.73 ^{-0.42}	28.38 \pm 0.42
ScribbleVC	71.45 \pm 1.92	14.14 \pm 4.12	70.98 \pm 2.22 ^{-0.47}	17.00 \pm 6.80
ScribFromer	61.90 \pm 4.96	29.41 \pm 10.40	61.42 \pm 1.33 ^{-0.48}	29.97 \pm 4.81
Ours	75.39 \pm 1.60	11.60 \pm 4.33	75.08 \pm 0.65^{-0.31}	12.07 \pm 0.48
	$\sigma = 0.10$		$\sigma = 0.15$	
U-Net + pCE	56.96 \pm 7.65 ^{-7.8}	31.36 \pm 2.30	40.95 \pm 13.83 ^{-23.81}	31.34 \pm 4.51
U-Net + USTM	51.78 \pm 4.59 ^{-13.04}	29.29 \pm 2.27	30.40 \pm 7.69 ^{-34.42}	24.89 \pm 4.18
U-Net + Gated CRF	73.06 \pm 0.56 ^{-1.81}	13.32 \pm 0.76	69.71 \pm 2.09 ^{-5.16}	17.85 \pm 5.98
DMPLS	59.55 \pm 2.82 ^{-6.55}	30.54 \pm 2.28	41.87 \pm 6.24 ^{-24.23}	32.96 \pm 6.61
ScribbleVC	68.98 \pm 5.19 ^{-2.47}	18.28 \pm 7.97	65.64 \pm 6.90 ^{-5.81}	21.62 \pm 8.45
ScribFromer	59.38 \pm 2.55 ^{-2.52}	32.03 \pm 6.46	55.97 \pm 6.62 ^{-5.93}	33.83 \pm 7.19
Ours	74.01 \pm 0.72^{-1.38}	13.04 \pm 1.02	71.58 \pm 1.31^{-3.81}	15.89 \pm 1.86

formance degradation was minimal, at just 3.81%. We observed significant disparities in model performance between the BUSI and CardiacUDA datasets, with models experiencing more pronounced performance degradation on BUSI as noise levels increase. We hypothesize that this could be attributed to the richer supervision information provided by the multi-class data. Given the larger number of classes, models may require learning more intricate features to represent the data, enabling them to better adapt and overcome the impact of noise. In summary, our method exhibited robustness due to the Dirichlet distribution’s capability to model probabilities of probabilities, essentially the confidence distribution of prediction outcomes across different classes. This approach offered greater flexibility by incorporating evidence theory to quantify prediction uncertainty, enabling the model to distinguish whether uncertainty stems from data noise or limitations in its own knowledge. This explicit modeling of uncertainty aided the model in maintaining stability when confronted with complex or anomalous inputs.

Furthermore, we visualized the uncertainty maps, as shown in Figs. 8 and 9. In most cases, the overall uncer-

tainty increased with the increment of noise. The model’s predictions tended to exhibit higher uncertainty at the edges of the target regions in individual images, while the internal regions of the targets generally showed lower uncertainty. As noise increased, some areas may be incorrectly predicted, but these regions typically manifested high uncertainty, observable from the figures. Notably, Fig. 9 revealed the notable impact of scribble annotations on some image predictions, with low uncertainty regions emerging around scribble annotations in background areas. This observation validated the effectiveness of our uncertainty estimation, as predictions within annotated regions should be highly evidential.

5. Conclusion

We have proposed a scribble-based WSL approach for ultrasound image segmentation, effectively reducing the annotation cost. The CNN-Mamba dual-branch networks that have been introduced effectively capture both local and global features while mitigating computational complexity. Moreover, the EDL-based EGC strategy that has

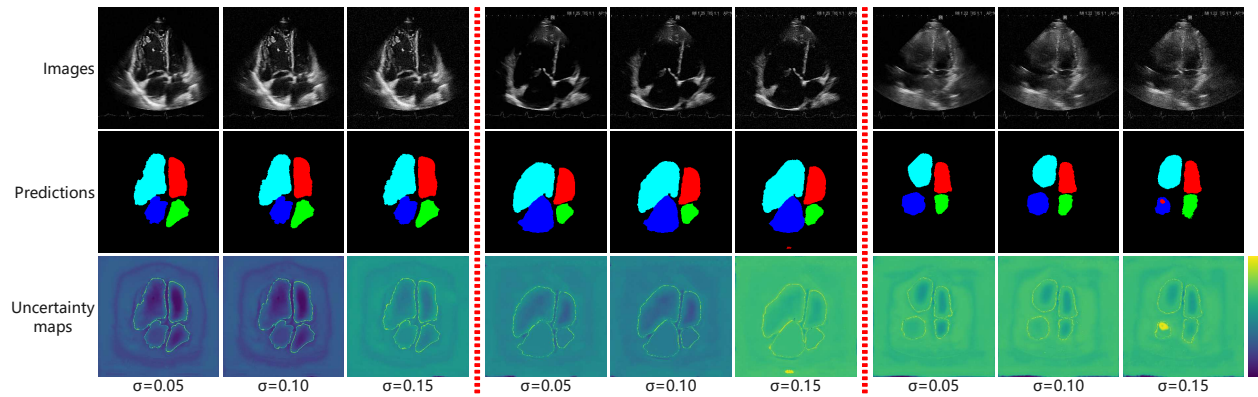


Figure 9: Visualization of the uncertainty map for the test results of our model on the CardiacUDA dataset. The symbol σ represents the standard deviation of the Gaussian noise added to the image.

been proposed refines the model’s prediction of edge regions, preserving and leveraging low-confidence pixels to enhance the stability of target edge prediction. Extensive experiments conducted on four public ultrasound image datasets have demonstrated that our method has exhibited superior performance in both binary and multi-class tasks, outperforming existing WSL approaches in terms of performance, generalization, and robustness. These accomplishments validate the effectiveness of our approach and its potential for clinical applications.

6. Acknowledgments

This work was supported by the National Natural Science Foundation of China (Grant No. 62071285), the Eastern Scholars Program from Shanghai Municipal Education Commission, and the Shanghai Technical Service Center of Science and Engineering Computing, Shanghai University.

References

- [1] Z. Wang, Deep learning in medical ultrasound image segmentation: a review, arXiv preprint arXiv:2002.07703 (2020).
- [2] K. He, X. Zhang, S. Ren, J. Sun, Deep residual learning for image recognition, in: Proceedings of the IEEE conference on computer vision and pattern recognition, 2016, pp. 770–778.
- [3] A. Vaswani, N. Shazeer, N. Parmar, J. Uszkoreit, L. Jones, A. N. Gomez, Ł. Kaiser, I. Polosukhin, Attention is all you need, *Advances in neural information processing systems* 30 (2017).
- [4] Y. Liu, X. Han, T. Liang, B. Dong, J. Yuan, M. Hu, Q. Liu, J. Chen, Q. Li, Y. Zhang, Edmae: An efficient decoupled masked autoencoder for standard view identification in pediatric echocardiography, *Biomedical Signal Processing and Control* 86 (2023) 105280.
- [5] O. Ronneberger, P. Fischer, T. Brox, U-net: Convolutional networks for biomedical image segmentation, in: *Medical image computing and computer-assisted intervention—MICCAI 2015: 18th international conference, Munich, Germany, October 5-9, 2015, proceedings, part III 18*, Springer, 2015, pp. 234–241.
- [6] H. Cao, Y. Wang, J. Chen, D. Jiang, X. Zhang, Q. Tian, M. Wang, Swin-unet: Unet-like pure transformer for medical image segmentation, in: *European conference on computer vision*, Springer, 2022, pp. 205–218.
- [7] W. Shen, Z. Peng, X. Wang, H. Wang, J. Cen, D. Jiang, L. Xie, X. Yang, Q. Tian, A survey on label-efficient deep image segmentation: Bridging the gap between weak supervision and dense pre-

- diction, *IEEE transactions on pattern analysis and machine intelligence* 45 (8) (2023) 9284–9305.
- [8] T. Zhao, Z. Yin, Weakly supervised cell segmentation by point annotation, *IEEE Transactions on Medical Imaging* 40 (10) (2020) 2736–2747.
- [9] X. Luo, M. Hu, W. Liao, S. Zhai, T. Song, G. Wang, S. Zhang, Scribble-supervised medical image segmentation via dual-branch network and dynamically mixed pseudo labels supervision, in: *International Conference on Medical Image Computing and Computer-Assisted Intervention*, Springer, 2022, pp. 528–538.
- [10] K. Han, V. S. Sheng, Y. Song, Y. Liu, C. Qiu, S. Ma, Z. Liu, Deep semi-supervised learning for medical image segmentation: A review, *Expert Systems with Applications* (2024) 123052.
- [11] L. Jing, Y. Tian, Self-supervised visual feature learning with deep neural networks: A survey, *IEEE transactions on pattern analysis and machine intelligence* 43 (11) (2020) 4037–4058.
- [12] N. Tajbakhsh, L. Jeyaseelan, Q. Li, J. N. Chiang, Z. Wu, X. Ding, Embracing imperfect datasets: A review of deep learning solutions for medical image segmentation, *Medical image analysis* 63 (2020) 101693.
- [13] K. Zhang, X. Zhuang, Cyclemix: A holistic strategy for medical image segmentation from scribble supervision, in: *Proceedings of the IEEE/CVF Conference on Computer Vision and Pattern Recognition*, 2022, pp. 11656–11665.
- [14] M. Han, X. Luo, W. Liao, S. Zhang, S. Zhang, G. Wang, Scribble-based 3d multiple abdominal organ segmentation via triple-branch multi-dilated network with pixel-and class-wise consistency, in: *International Conference on Medical Image Computing and Computer-Assisted Intervention*, Springer, 2023, pp. 33–42.
- [15] S. Adiga, J. Dolz, H. Lombaert, Anatomically-aware uncertainty for semi-supervised image segmentation, *Medical Image Analysis* 91 (2024) 103011.
- [16] J. Yang, X. Ding, Z. Zheng, X. Xu, X. Li, Graphecho: Graph-driven unsupervised domain adaptation for echocardiogram video segmentation, in: *Proceedings of the IEEE/CVF International Conference on Computer Vision*, 2023, pp. 11878–11887.
- [17] D. Ouyang, B. He, A. Ghorbani, N. Yuan, J. Ebinger, C. P. Langlotz, P. A. Heidenreich, R. A. Harrington, D. H. Liang, E. A. Ashley, et al., Video-based ai for beat-to-beat assessment of cardiac function, *Nature* 580 (7802) (2020) 252–256.
- [18] W. Al-Dhabyani, M. Goma, H. Khaled, A. Fahmy, Dataset of breast ultrasound images, *Data in brief* 28 (2020) 104863.
- [19] L. Pedraza, C. Vargas, F. Narváez, O. Durán, E. Muñoz, E. Romero, An open access thyroid ultrasound image database, in: *10th International symposium on medical information processing and analysis*, Vol. 9287, SPIE, 2015, pp. 188–193.
- [20] M. Y. Ansari, I. A. C. Mangalote, P. K. Meher, O. Aboumarzouk, A. Al-Ansari, O. Halabi, S. P. Dakua, Advancements in deep learning for b-mode ultrasound segmentation: A comprehensive review, *IEEE Transactions on Emerging Topics in Computational Intelligence* (2024).
- [21] S. Leclerc, E. Smistad, J. Pedrosa, A. Østvik, F. Cervenansky, F. Espinosa, T. Espeland, E. A. R. Berg, P.-M. Jodoin, T. Grenier, et al., Deep learning for segmentation using an open large-scale dataset in 2d echocardiography, *IEEE transactions on medical imaging* 38 (9) (2019) 2198–2210.
- [22] Y. Shen, H. Zhang, Y. Fan, A. P. Lee, L. Xu, Smart health of ultrasound telemedicine based on deeply represented semantic segmentation, *IEEE Internet of Things Journal* 8 (23) (2020) 16770–16778.
- [23] L. Xu, M. Liu, J. Zhang, Y. He, Convolutional-neural-network-based approach for segmentation of apical four-chamber view from fetal echocardiography, *IEEE Access* 8 (2020) 80437–80446.
- [24] F. Liu, K. Wang, D. Liu, X. Yang, J. Tian, Deep pyramid local attention neural network for cardiac

- structure segmentation in two-dimensional echocardiography, *Medical image analysis* 67 (2021) 101873.
- [25] X. Li, S. Pang, R. Zhang, J. Zhu, X. Fu, Y. Tian, J. Gao, Attransunet: An enhanced hybrid transformer architecture for ultrasound and histopathology image segmentation, *Computers in Biology and Medicine* 152 (2023) 106365.
- [26] J. Chi, Z. Li, Z. Sun, X. Yu, H. Wang, Hybrid transformer unet for thyroid segmentation from ultrasound scans, *Computers in Biology and Medicine* 153 (2023) 106453.
- [27] L. Zhao, G. Tan, B. Pu, Q. Wu, H. Ren, K. Li, Transfm: Fetal anatomy segmentation and biometric measurement in ultrasound images using a hybrid transformer, *IEEE Journal of Biomedical and Health Informatics* (2023).
- [28] H. Yang, D. Yang, Cswin-pnet: A cnn-swin transformer combined pyramid network for breast lesion segmentation in ultrasound images, *Expert Systems with Applications* 213 (2023) 119024.
- [29] A. Gu, T. Dao, Mamba: Linear-time sequence modeling with selective state spaces, *arXiv preprint arXiv:2312.00752* (2023).
- [30] J. Ma, F. Li, B. Wang, U-mamba: Enhancing long-range dependency for biomedical image segmentation, *arXiv preprint arXiv:2401.04722* (2024).
- [31] J. Ruan, S. Xiang, Vm-unet: Vision mamba unet for medical image segmentation, *arXiv preprint arXiv:2402.02491* (2024).
- [32] Z. Ye, T. Chen, P-mamba: Marrying perona malik diffusion with mamba for efficient pediatric echocardiographic left ventricular segmentation, *arXiv preprint arXiv:2402.08506* (2024).
- [33] A. Nasiri-Sarvi, M. S. Hosseini, H. Rivaz, Vision mamba for classification of breast ultrasound images, *arXiv preprint arXiv:2407.03552* (2024).
- [34] Z. Ye, T. Chen, D. Wang, F. Wang, L. Zhang, Hfemamba: High-frequency enhanced mamba network for efficient segmentation of left ventricle in pediatric echocardiograms, *IEEE Access* (2024).
- [35] V. Kulharia, S. Chandra, A. Agrawal, P. Torr, A. Tyagi, Box2seg: Attention weighted loss and discriminative feature learning for weakly supervised segmentation, in: *European Conference on Computer Vision*, Springer, 2020, pp. 290–308.
- [36] D. Lin, J. Dai, J. Jia, K. He, J. Sun, Scribblesup: Scribble-supervised convolutional networks for semantic segmentation, in: *Proceedings of the IEEE conference on computer vision and pattern recognition*, 2016, pp. 3159–3167.
- [37] A. Obukhov, S. Georgoulis, D. Dai, L. Van Gool, Gated crf loss for weakly supervised semantic image segmentation, *arXiv preprint arXiv:1906.04651* (2019).
- [38] H. Lee, W.-K. Jeong, Scribble2label: Scribble-supervised cell segmentation via self-generating pseudo-labels with consistency, in: *Medical Image Computing and Computer Assisted Intervention—MICCAI 2020: 23rd International Conference, Lima, Peru, October 4–8, 2020, Proceedings, Part I 23*, Springer, 2020, pp. 14–23.
- [39] Z. Li, Y. Zheng, X. Luo, D. Shan, Q. Hong, Scribblevc: Scribble-supervised medical image segmentation with vision-class embedding, in: *Proceedings of the 31st ACM International Conference on Multimedia*, 2023, pp. 3384–3393.
- [40] Z. Li, Y. Zheng, D. Shan, S. Yang, Q. Li, B. Wang, Y. Zhang, Q. Hong, D. Shen, Scribformer: Transformer makes cnn work better for scribble-based medical image segmentation, *IEEE Transactions on Medical Imaging* (2024).
- [41] Z. Pan, P. Jiang, Y. Wang, C. Tu, A. G. Cohn, Scribble-supervised semantic segmentation by uncertainty reduction on neural representation and self-supervision on neural eigenspace, in: *Proceedings of the IEEE/CVF International Conference on Computer Vision*, 2021, pp. 7416–7425.
- [42] X. Liu, Q. Yuan, Y. Gao, K. He, S. Wang, X. Tang, J. Tang, D. Shen, Weakly supervised segmentation

of covid19 infection with scribble annotation on ct images, *Pattern recognition* 122 (2022) 108341.

- [43] M. Sensoy, L. Kaplan, M. Kandemir, Evidential deep learning to quantify classification uncertainty, *Advances in neural information processing systems* 31 (2018).
- [44] A. Jsang, *Subjective Logic: A formalism for reasoning under uncertainty*, Springer Publishing Company, Incorporated, 2018.
- [45] Y. Chen, Z. Yang, C. Shen, Z. Wang, Y. Qin, Y. Zhang, Evil: Evidential inference learning for trustworthy semi-supervised medical image segmentation, in: *2023 IEEE 20th International Symposium on Biomedical Imaging (ISBI)*, IEEE, 2023, pp. 1–5.
- [46] Z. Wang, J.-Q. Zheng, Y. Zhang, G. Cui, L. Li, Mamba-unet: Unet-like pure visual mamba for medical image segmentation, *arXiv preprint arXiv:2402.05079* (2024).
- [47] A. Gu, K. Goel, C. Ré, Efficiently modeling long sequences with structured state spaces, *arXiv preprint arXiv:2111.00396* (2021).
- [48] Y. Liu, Y. Tian, Y. Zhao, H. Yu, L. Xie, Y. Wang, Q. Ye, Y. Liu, Vmamba: Visual state space model, *arXiv preprint arXiv:2401.10166* (2024).
- [49] Y. Wang, H. Chen, Q. Heng, W. Hou, Y. Fan, Z. Wu, J. Wang, M. Savvides, T. Shinozaki, B. Raj, et al., Freematch: Self-adaptive thresholding for semi-supervised learning, *arXiv preprint arXiv:2205.07246* (2022).
- [50] X. Chen, Y. Yuan, G. Zeng, J. Wang, Semi-supervised semantic segmentation with cross pseudo supervision, in: *Proceedings of the IEEE/CVF conference on computer vision and pattern recognition*, 2021, pp. 2613–2622.
- [51] M. Tang, A. Djelouah, F. Perazzi, Y. Boykov, C. Schroers, Normalized cut loss for weakly-supervised cnn segmentation, in: *Proceedings of the IEEE conference on computer vision and pattern recognition*, 2018, pp. 1818–1827.